

Strong Conformity and Assembly Bias: Towards a Physical Understanding of the Galaxy-Halo Connection in SDSS Clusters

Ying Zu^{1,2*}, Yunjia Song¹, Zhiwei Shao¹, Xiaokai Chen¹, Yun Zheng¹, Hongyu Gao¹,
Yu Yu^{1,2}, Huanyuan Shan³, Yipeng Jing^{1,2,4}

¹Department of Astronomy, School of Physics and Astronomy, Shanghai Jiao Tong University, Shanghai 200240, China

²Shanghai Key Laboratory for Particle Physics and Cosmology, Shanghai Jiao Tong University, Shanghai 200240, China

³Key Laboratory for Research in Galaxies and Cosmology, Shanghai Astronomical Observatory, Shanghai 200030, China

⁴Tsung-Dao Lee Institute, Shanghai Jiao Tong University, Shanghai, 200240, China

Accepted XXX. Received YYY; in original form ZZZ

ABSTRACT

Understanding the physical connection between cluster galaxies and massive haloes is key to mitigating systematic uncertainties in next-generation cluster cosmology. We develop a novel method to infer the level of conformity between the stellar mass of the bright central galaxies (BCGs) M_*^{BCG} and the satellite richness λ , defined as their correlation coefficient ρ_{cc} at fixed halo mass, using the abundance and weak lensing of SDSS clusters as functions of M_*^{BCG} and λ . We detect a halo mass-dependent conformity as $\rho_{\text{cc}}=0.60+0.08 \ln(M_h/3\times 10^{14} h^{-1} M_\odot)$. The strong conformity successfully resolves the “halo mass equality” conundrum discovered in Zu et al. (2021) — when split by M_*^{BCG} at fixed λ , the low and high- M_*^{BCG} clusters have the same average halo mass despite having a 0.34 dex discrepancy in average M_*^{BCG} . On top of the best-fitting conformity model, we develop a cluster assembly bias (AB) prescription calibrated against the CosmicGrowth simulation, and build a conformity+AB model for the cluster weak lensing measurements. Our model predicts that with a $\sim 20\%$ lower halo concentration c , the low- M_*^{BCG} clusters are $\sim 10\%$ more biased than the high- M_*^{BCG} systems, in good agreement with the observations. We also show that the observed conformity and assembly bias are unlikely due to projection effects. Finally, we build a toy model to argue that while the early-time BCG-halo co-evolution drives the $M_*^{\text{BCG}}-c$ correlation, the late-time dry merger-induced BCG growth naturally produces the $M_*^{\text{BCG}}-\lambda$ conformity despite the well-known anti-correlation between λ and c . Our method paves the path towards simultaneously constraining cosmology and cluster formation with future cluster surveys.

Key words: galaxies: evolution — galaxies: formation — galaxies: abundances — galaxies: statistics — cosmology: large-scale structure of Universe

1 INTRODUCTION

Collapsed from the highest peaks in the initial matter density field, galaxy clusters are one of the most sensitive probes of cosmic growth (see §6 of Weinberg et al. 2013, for a comprehensive review). With the advent of all-sky optical imaging surveys, the abundance of clusters with accurate halo mass measurements from weak gravitational lensing provides stringent constraints on the matter density Ω_m and clustering amplitude σ_8 (Roza et al. 2010; Zu et al. 2014a; Abbott et al. 2020), the total mass of the neutrinos (Carbone et al. 2012; Costanzi Alunno Cerbolini et al. 2013; Sartoris et al. 2016), and the nature of gravity (Lam et al. 2012; Zu et al. 2014b; Cataneo & Rapetti 2018). However, cosmology with optical clusters requires a thorough understanding of the connection between dark matter haloes and cluster member galaxies, including both the satellite galaxies and

the bright central galaxies (BCGs¹). In this paper, we investigate the level of BCG-satellite conformity and cluster assembly bias for a large sample of clusters observed by the Sloan Digital Sky Survey (SDSS; York et al. 2000), in hopes of developing a comprehensive model for interpreting the weak lensing of clusters (Mandelbaum 2018; Umetsu 2020) in next-generation imaging surveys.

The “conformity” phenomenon was originally detected by Weinmann et al. (2006) inside the SDSS galaxy groups (Yang et al. 2007). They found that the early-type fraction of satellite galaxies is significantly higher in a halo with an early-type central than in a halo of the same mass but with a late-type central. Similar group-scale conformities were reported for neutral gas fraction (Kauffmann et al. 2010), emission features (Robotham et al. 2013), and quenching efficiency (Phillips et al. 2014; Knobel et al. 2015). Such a conformity

¹ We deliberately avoid the more commonly-used nomenclature of “brightest cluster galaxies” as BCGs, because we are interested in the properties of the central galaxies, which are not necessarily the brightest members in their host clusters (Chen et al. 2021).

* E-mail: yingzu@sjtu.edu.cn

at fixed halo mass suggests that a secondary halo property (e.g., halo concentration; [Paranjape et al. 2015](#); [Zu & Mandelbaum 2018](#)) affected the galaxy evolution within clusters regardless of the central vs. satellite dichotomy. However, by applying a group-finding algorithm to a conformity-free galaxy mock, [Calderon et al. \(2018\)](#) demonstrated that the conformity signal could be spurious and likely entirely caused by group-finding systematics.

For more massive systems, a conformity likely exists between the BCG stellar mass (M_*^{BCG}) and the richness of massive satellite galaxies (λ), as physical processes that tie the stellar mass growth of the BCGs to the BCG-satellite interactions could naturally produce more massive BCGs in richer clusters at fixed halo mass. For instance, galactic cannibalism predicts that BCGs grow primarily from dissipationless mergers with satellite galaxies that were already in place at $z=2$ ([White 1976](#); [Ostriker & Hausman 1977](#)), and BCGs could also grow their outskirts via the accretion of tidally disrupted satellites ([Wetzel & White 2010](#)). Observationally, [Liu et al. \(2009\)](#) found that the fraction of BCGs in major dry mergers increases with the richness of the clusters; [To et al. \(2020\)](#) inferred a positive correlation between the BCG luminosity and λ from analyzing the central and satellite luminosity functions of SDSS clusters. However, they speculated that the correlation may be induced by the projection effects ([Zu et al. 2017](#); [Busch & White 2017](#); [Costanzi et al. 2019a](#); [Sunayama et al. 2020](#); [Myles et al. 2021](#); [Grandis et al. 2021](#)), which could boost the estimated richness for clusters in denser environments, hence earlier formation times and somewhat brighter BCGs.

More recently, [Zu et al. \(2021\)](#), hereafter referred to as [Paper I](#)) measured the weak lensing signals $\Delta\Sigma$ for two subsamples of SDSS clusters, split by M_*^{BCG} at fixed λ . They discovered that the two subsamples have equal average halo mass, despite having a ~ 0.34 dex discrepancy in M_*^{BCG} . This apparent M_*^{BCG} -independence of halo mass is intriguing, as models of cluster formation robustly predict that the average halo mass is an increasing function of BCG stellar mass, with more massive BCGs generally occupying haloes of higher mass. Therefore, for such a “halo mass equality” to be observed between the low and high- M_*^{BCG} clusters with the same λ distribution, we expect a non-trivial correlation between M_*^{BCG} and λ at fixed halo mass, i.e., a conformity or anti-conformity between the BCG and satellite galaxies.

Interestingly, [Paper I](#) also found that the high- M_*^{BCG} clusters have a higher average halo concentration and a lower halo bias, compared to their low- M_*^{BCG} counterparts with the same average halo mass. This concentration–bias relation is potentially a detection of the “cluster assembly bias” phenomenon, which was robustly predicted by Λ CDM simulations ([Gao et al. 2005](#); [Jing et al. 2007](#)). In principle, we can measure the average halo mass and concentration from the small-scale $\Delta\Sigma$, as well as the average halo bias from $\Delta\Sigma$ on large scales. However, previous studies focused primarily on the measurement of halo mass from the small-scale $\Delta\Sigma$, while the concentration-bias relation encoded in $\Delta\Sigma$ is largely unexplored due to their relatively large measurement uncertainties from weak lensing. To extract unbiased cosmological information from cluster weak lensing, it is imperative that we incorporate the cluster assembly bias effect into the modelling of $\Delta\Sigma$ measurements from upcoming surveys with much smaller statistical uncertainties.

In this paper, we will firstly explore the “halo mass equality” conundrum discovered in [Paper I](#) by explicitly modelling the correlation between M_*^{BCG} and λ at fixed halo mass M_h , and then develop a cluster assembly bias prescription for a simple yet comprehensive model of cluster weak lensing. Our paper is accordingly organised into two main parts. In the first part of the paper, we describe the cluster catalogue, BCG stellar mass estimates, and weak lensing measure-

ments in §2. The statistical model of BCG–satellite conformity and the Bayesian inference method are described in §3. We present our model constraints and our solution to the “halo mass equality” conundrum in §4. In the second part of the paper, we develop a novel model for the cluster weak lensing by including both conformity and assembly bias in §5, supplemented by the Appendices §A and §B. We discuss the physical implications of our findings in §6 and conclude by summarising our results and looking to the future in §7.

Throughout this paper, we assume the *Planck* cosmology ([Planck Collaboration et al. 2020](#)). All the length and mass units in this paper are scaled as if the Hubble constant is $100 \text{ km s}^{-1} \text{ Mpc}^{-1}$. In particular, all the separations are co-moving distances in units of $h^{-1} \text{ Mpc}$, and the halo and stellar mass are in units of $h^{-1} M_\odot$ and $h^{-2} M_\odot$, respectively. We adopt a spherical overdensity-based halo definition so that the average halo density with the halo radius r_{200m} is 200 times the mean density of the Universe, and the mass enclosed within r_{200m} is the halo mass M_h . We use $\lg x = \log_{10} x$ for the base-10 logarithm and $\ln x = \log_e x$ for the natural logarithm.

2 DATA

2.1 Cluster Catalogue and Stellar Mass Estimates

Following [Paper I](#), we employ the SDSS redMaPPer cluster catalogue ([Rykoff et al. 2014](#)) derived by applying a red-sequence-based photometric cluster finding algorithm to the SDSS DR8 imaging ([Aihara et al. 2011](#)). Briefly, redMaPPer iteratively self-trains a model of red-sequence galaxies calibrated by an input spectroscopic galaxy sample, and then attempts to grow a galaxy cluster centred about every photometric galaxy. Once a galaxy cluster has been identified by the matched-filters, the algorithm iteratively solves for a photometric redshift based on the calibrated red-sequence model, and re-centres the clusters about the best BCG candidates.

Therefore, each redMaPPer cluster is a conglomerate of red-sequence galaxies on the sky, with each galaxy assigned a membership probability p_{mem} and a probability of being the BCG p_{cen} . For each cluster, the richness λ was computed by summing the p_{mem} of all member galaxy candidates, and roughly corresponds to the number of red-sequence satellite galaxies brighter than $0.2 L_*$ within an aperture of $\sim 1 h^{-1} \text{ Mpc}$ (with a weak dependence on λ). At $\lambda \geq 20$, the SDSS redMaPPer cluster catalogue is approximately volume-complete up to $z \approx 0.33$, with cluster photometric redshift uncertainties as small as $\delta(z) = 0.006/(1+z)$ ([Rykoff et al. 2014](#); [Roza et al. 2015](#)).

We select 5476 clusters with $\lambda \geq 20$ and redshifts between 0.17 and 0.30 ($\langle z \rangle = 0.242$) over a sky area of 10401 deg^2 , and pick the galaxy with the highest p_{cen} in each cluster as the BCG. Among the 5476 BCGs, 3610 of them (66 per cent) have spectroscopic redshifts from SDSS, and for the 1866 BCGs without spectroscopy we assign them the photometric redshifts of their host clusters. We include 909 more clusters than in [Paper I](#) (4567 clusters), which excluded the area that was masked out by the BOSS LOWZ galaxy sample ([Dawson et al. 2013](#); [Alam et al. 2015](#)).

Following [Paper I](#), we derive stellar masses for all BCGs by fitting a two-component Simple Stellar Population (SSP) template to their extinction-corrected *gri* model magnitudes (scaled to the *i*-band *c*-model magnitudes). Following [Maraston et al. \(2009\)](#), we assume the dominant stellar population (97 per cent) to be solar metallicity, supplemented with a secondary (3 per cent) metal-poor ($Z=0.008$) population of the same age. We utilize the EzGal software ([Mancone & Gonzalez 2012](#)) and adopt the [Bruzual & Charlot \(2003\)](#) SSP

Table 1. Weak lensing mass estimates (and associated uncertainties) of the redMaPPer clusters binned by λ , derived from [Simet et al. \(2017\)](#). We assume 50 per cent of the uncertainties are systematic errors.

λ	[20,30)	[30,40)	[40,55)	[55, 100)
$\lg M_h$	14.05±0.05	14.25±0.05	14.43±0.05	14.64±0.05

model and the [Chabrier \(2003\)](#) IMF for the fits. By examining the stacked surface stellar mass density profiles of clusters at fixed M_*^{BCG} , we infer the effective aperture of our M_*^{BCG} estimates to be about $35 h^{-1} \text{kpc}$ ([Chen et al. 2021](#)). For a detailed comparison between our photometric stellar mass estimates and the spectroscopic stellar masses from [Chen et al. \(2012\)](#), we refer interested readers to the Figure 1 in [Paper I](#).

However, there exists a systematic uncertainty in our central galaxy stellar mass measurement due to the mis-centring effect, i.e., some of the BCGs identified by the maximum p_{cen} are actually satellite galaxies ([Zhang et al. 2019](#)). From the weak lensing analysis, [Paper I](#) inferred that $\sim 30\%$ of the redMaPPer clusters in our sample are mis-centred, and the mis-centring fraction decreases with increasing M_*^{BCG} . To assess the size of the systematic bias induced by mis-centring, we examine the distribution of the stellar mass gaps ΔM_*^{BCG} between galaxies with the maximum (i.e. our BCG candidates) and second highest p_{cen} in individual clusters. We find that in 25% of the clusters the second probable central is more massive than the BCG we select, and that among those clusters with $\Delta M_*^{\text{BCG}} < 0$, 70% of them have $\Delta M_*^{\text{BCG}} > -0.1$ dex. Therefore, assuming that the mis-centred clusters are likely those with negative stellar mass gaps, we expect that the BCG stellar mass of the mis-centred clusters could be systematically underestimated by ~ 0.05 – 0.1 dex.

2.2 Cluster Weak Lensing Measurements

We employ two sets of cluster weak lensing measurements in our analysis. For the Bayesian analysis in §4, we derive constraints on $p(M_*^{\text{BCG}}, \lambda | M_h)$, the 2D probability density function (PDF) of the M_*^{BCG} and λ of clusters at fixed M_h , by making use of the weak lensing halo mass measurements of clusters in bins of λ from [Simet et al. \(2017\)](#). In particular, we assume the best-fitting mass–richness relation inferred by [Simet et al. \(2017\)](#) (their Equation 28), and compute the mean halo mass in each of the four richness bins, which is listed in Table 1. Following [Simet et al. \(2017\)](#) (also see [Costanzi et al. 2019b](#)), we assign 50 per cent of the uncertainties as systematic errors, which we assume to be fully correlated between different richness bins. [Murata et al. \(2018\)](#) showed that the mass–richness relation of [Simet et al. \(2017\)](#) derived from the SDSS imaging is consistent with the recent measurements from the Hyper Suprime-Cam (HSC; [Aihara et al. 2018](#); [Mandelbaum et al. 2018](#)). We refer interested readers to [Simet et al. \(2017\)](#) for technical details of the halo mass measurements.

For testing whether our best-fitting models of $p(M_*^{\text{BCG}}, \lambda | M_h)$, in combination with the cluster assembly bias prescription, can resolve the “halo mass equality” conundrum, we predict the surface density contrast profiles $\Delta\Sigma(r_p)$ for the low and high- M_*^{BCG} cluster subsamples, and compare to the weak lensing measurements of the two subsamples made in [Paper I](#) from the DECaLS imaging ([Dey et al. 2019](#)). We will directly present the comparison in §5 and refer readers to [Paper I](#) for technical details of the weak lensing measurements from DECaLS.

Note that we do not include the halo mass estimates for the low

and high- M_*^{BCG} clusters from [Paper I](#) in our Bayesian analysis of §4, because the estimates from [Paper I](#) do not include some of the systematic uncertainties considered by [Simet et al. \(2017\)](#), including the shear calibration errors, photo-z biases, halo triaxiality, etc. Therefore, to avoid inhomogeneity in our input data, we only include the weak lensing halo mass in bins of λ measured by [Simet et al. \(2017\)](#) in our Bayesian analysis, but directly model the $\Delta\Sigma$ measurements from [Paper I](#) in §5.

3 METHODOLOGY

The data vector of our Bayesian analysis in §4 consists of three components,

- $N_{\text{cls}} = 5476$: the total number of clusters observed with $\lambda \geq 20$ and $0.17 < z < 0.30$ over a sky area of 10401 deg^2 .
- $\{M_*^{\text{BCG}}, \lambda\}_{i=1 \dots 5476}$: BCG stellar mass and satellite richness of the observed 5476 individual clusters.
- $\{M_h | [\lambda_{\text{min}}^j, \lambda_{\text{max}}^j]\}_{j=1 \dots 4}$: Weak lensing halo mass measurements of four richness bins listed in Table 1.

Below we will describe our analytic model for predicting each of the three components.

3.1 Modelling the 2D PDF of M_*^{BCG} and λ at fixed M_h

The 2D PDF of M_*^{BCG} and λ at fixed M_h , $p(M_*^{\text{BCG}}, \lambda | M_h)$, is the centrepiece of our statistical model of galaxy-halo connection for clusters. Our model of $p(M_*^{\text{BCG}}, \lambda | M_h)$ consists of three components, the richness-to-halo mass relation (RHMR) that describes the 1D log-normal PDF of richness at fixed halo mass $p(\lambda | M_h)$, the stellar-to-halo mass relation (SHMR) that specifies the 1D log-normal PDF of BCG stellar mass at fixed halo mass $p(M_*^{\text{BCG}} | M_h)$, and the correlation coefficient between M_*^{BCG} and λ as a function of halo mass $\rho_{\text{cc}}(M_h)$. We will refer to models with $\rho_{\text{cc}} > 0$ as “conformity” models and those with $\rho_{\text{cc}} < 0$ as “anti-conformity” models, respectively.

We assume the mean RHMR to be

$$\langle \ln \lambda | M_h \rangle = A + \alpha \ln \left(\frac{M_h}{M_{\text{pivot}}} \right), \quad (1)$$

where A and α are the amplitude and slope of the power-law, respectively, and we set the pivot halo mass $M_{\text{pivot}} = 3 \times 10^{14} h^{-1} M_{\odot}$. Following [Murata et al. \(2018\)](#), we further assume a mass-dependent logarithmic scatter about the median RHMR,

$$\sigma_{\ln \lambda | M_h} = \sigma_{\ln \lambda, 0} + q \ln \left(\frac{M_h}{M_{\text{pivot}}} \right), \quad (2)$$

where $\sigma_{\ln \lambda, 0}$ is the scatter at M_{pivot} , and q is the slope of the halo mass dependence. The combination of Equations 1 and 2 thus fully describes the RHMR

$$p(\ln \lambda | M_h) \sim \mathcal{N} \left(\langle \ln \lambda | M_h \rangle, \sigma_{\ln \lambda | M_h}^2 \right). \quad (3)$$

For the mean SHMR, we adopt a functional form proposed by [Behroozi et al. \(2010\)](#) via its inverse function,

$$M_h = M_1 m^{\beta} 10^{(m^{\delta}/(1+m^{-\gamma})-1/2)}, \quad (4)$$

where $m \equiv M_*/M_{*,0}$. Among the five parameters in Equation 4, $M_{h,1}$ and $M_{*,0}$ are the characteristic halo mass and stellar mass that separate the behaviours in the low and high mass ends. The inverse function starts with a low-mass end slope β , crosses a transitional regime around $(M_{*,0}, M_{h,1})$ dictated by γ , and reaches a high-mass end slope $\beta+\delta$. We assume a constant log-normal scatter $\sigma_{\ln M_*^{\text{BCG}} | M_h}$,

because we are primarily interested in the massive end of the SHMR, where the halo mass dependence of scatter was found to be weak (Zu & Mandelbaum 2015). Similarly, the combination of Equations 4 and a constant scatter fully specifies the SHMR

$$p(\ln M_*^{\text{BCG}} | M_h) \sim \mathcal{N}(\langle \ln M_*^{\text{BCG}} | M_h \rangle, \sigma_{\ln M_*^{\text{BCG}} | M_h}^2). \quad (5)$$

As mentioned in §1, Paper I discovered that the scatter of the SHMR is at least partially driven by the concentration of dark matter haloes, so that the more massive BCGs are preferentially hosted by the more concentrated haloes at fixed halo mass. Therefore, to accurately predict the weak lensing profiles of clusters binned by M_*^{BCG} , we also need to take into account the concentration–bias relation predicted by the halo assembly bias effect, as will be discussed later in §5.

To derive the joint 2D PDF $p(M_*^{\text{BCG}}, \lambda | M_h)$, we need to combine Equation 3 and 5 into a bivariate Gaussian at each halo mass via the correlation coefficient ρ_{cc} at that mass. To allow the level of conformity between BCG and satellites to vary with halo mass, we assume a halo mass dependence of ρ_{cc} as

$$\rho_{cc}(M_h) = \rho_{cc,0} + s \ln \left(\frac{M_h}{M_{\text{pivot}}} \right), \quad (6)$$

where $\rho_{cc,0}$ is the correlation coefficient at M_{pivot} , and s describes the slope of the halo mass dependence. Given the two mean scaling relations and their associated scatters, it is now trivial to write out the bivariate Gaussian form for $p(\ln M_*^{\text{BCG}}, \ln \lambda | M_h)$ as

$$p(\ln M_*^{\text{BCG}}, \ln \lambda | M_h) = \frac{\exp\left(-(\hat{l}^2 - 2\rho_{cc}\hat{l}\hat{m}_* + \hat{m}_*^2)/(2(1 - \rho_{cc}^2))\right)}{2\pi\sigma_{\ln \lambda | M_h}\sigma_{\ln M_*^{\text{BCG}} | M_h}\sqrt{1 - \rho_{cc}^2}}, \quad (7)$$

where \hat{m}_* is the *relative* BCG stellar mass

$$\hat{m}_* \equiv \frac{\ln M_*^{\text{BCG}} - \langle \ln M_*^{\text{BCG}} | M_h \rangle}{\sigma_{\ln M_*^{\text{BCG}} | M_h}}, \quad (8)$$

and $\hat{\lambda}$ the *relative* richness

$$\hat{\lambda} \equiv \frac{\ln \lambda - \langle \ln \lambda | M_h \rangle}{\sigma_{\ln \lambda | M_h}}. \quad (9)$$

3.2 Predicting Observing Probability of Each Cluster

To predict the probability of observing any cluster with BCG mass M_*^{BCG} and satellite richness λ , we integrate $p(M_*^{\text{BCG}}, \lambda | M_h)$ over the halo mass function to obtain

$$p(\ln M_*^{\text{BCG}}, \ln \lambda) = \frac{1}{n_0} \int_{M_h^{\min}}^{M_h^{\max}} p(\ln M_*^{\text{BCG}}, \ln \lambda | M_h) \frac{dn}{dM_h} dM_h, \quad (10)$$

where dn/dM_h is the halo mass function at *Planck* cosmology, and n_0 is the total number density of haloes between M_h^{\min} and M_h^{\max} . We choose the two integration limits to be $5 \times 10^{11} h^{-1} M_\odot$ and $10^{16} h^{-1} M_\odot$, respectively, and adopt the Tinker et al. (2008) fitting formula for dn/dM_h . With the integration limits (hence n_0) fixed, we can set $p(M_h) \equiv dn/dM_h/n_0$ for the rest of the paper. Note that although we evaluate all the quantities at each of the six equal-width redshift slices between $z=0.17$ and 0.30 , and integrate over the redshift range (with cluster photo- z uncertainty included) to obtain our final predictions, we omit z in the equations whenever possible to avoid clutter in the math.

3.3 Predicting Halo Mass Distribution of Each Cluster

To reveal the underlying dark matter halo population of each subsample of clusters binned by M_*^{BCG} and (or) λ , we need to predict the halo mass distribution of each cluster observed with M_*^{BCG} and λ . Using Bayes' theorem, we can write the PDF of halo mass as

$$p(M_h | M_*^{\text{BCG}}, \lambda) = \frac{p(M_*^{\text{BCG}}, \lambda, M_h)}{p(M_*^{\text{BCG}}, \lambda)} = \frac{p(M_*^{\text{BCG}}, \lambda | M_h) p(M_h)}{p(M_*^{\text{BCG}}, \lambda)}, \quad (11)$$

using Equations 7, 10, and $p(M_h)$.

Similarly, if we select clusters just by their richness, the PDF of halo mass is simply

$$p(M_h | \lambda) = \frac{p(\lambda | M_h) p(M_h)}{p(\lambda)}, \quad (12)$$

where

$$p(\lambda) = \int_{M_h^{\min}}^{M_h^{\max}} p(\lambda | M_h) p(M_h) dM_h. \quad (13)$$

Therefore, the total number of $\lambda \geq 20$ clusters within $z_{\min}=0.17$ and $z_{\max}=0.30$ over a sky area Ω is

$$\langle N \rangle = \frac{n_0 \Omega}{4\pi} \int_{z_{\min}}^{z_{\max}} \frac{dV}{dz} \int_{\lambda_{\min}=20} p(\lambda | z) d\lambda. \quad (14)$$

More generically, we can compute the halo mass distribution of any set of N clusters as

$$p(M_h | \{M_*^{\text{BCG}}, \lambda\}_{i=1 \dots N}) = \frac{1}{N} \sum_{i=1}^N p(M_h | \{M_*^{\text{BCG}}, \lambda\}_i), \quad (15)$$

and then we can predict the average halo mass of the same set of N clusters as

$$\langle M_h | \{M_*^{\text{BCG}}, \lambda\}_{i=1 \dots N} \rangle = \int p(M_h | \{M_*^{\text{BCG}}, \lambda\}_{i=1 \dots N}) M_h dM_h. \quad (16)$$

In particular, we predict the average halo mass of clusters with $\lambda \in [\lambda_{\min}^j, \lambda_{\max}^j]$ by evaluating Equations 15 and 16 over the N_j clusters in each of the four richness bins in Table 1.

4 BAYESIAN INFERENCE: A TALE OF TWO CONFORMITY MODELS

4.1 Model Degeneracy: Conformity vs. Anti-conformity

Before moving on to the Bayesian inference of model parameters, we illustrate in Figure 1 that there exists a strong degeneracy in our current model so that both conformity and anti-conformity models can describe the 2D abundance of clusters and the weak lensing halo mass in bins of richness, with exactly the same RHMR but different SHMRs.

In the top left panel of Figure 1, the red solid and blue dashed lines are the mean RHMRs of the conformity and anti-conformity models, respectively, with horizontally and vertically hatched bands of the same colours indicating their corresponding scatters. The two RHMRs are exactly the same by design, so that the two models will predict exactly the same average halo mass for any cluster sample binned in richness (as shown in Panel *dI*). The minimum richness cut of 20 is indicated by the gray horizontal line. In the top right panel of Figure 1, we adopt the same plotting styles for the conformity vs. anti-conformity models as in the top left panel, but show the SHMRs instead. The SHMR of the conformity model (red solid line

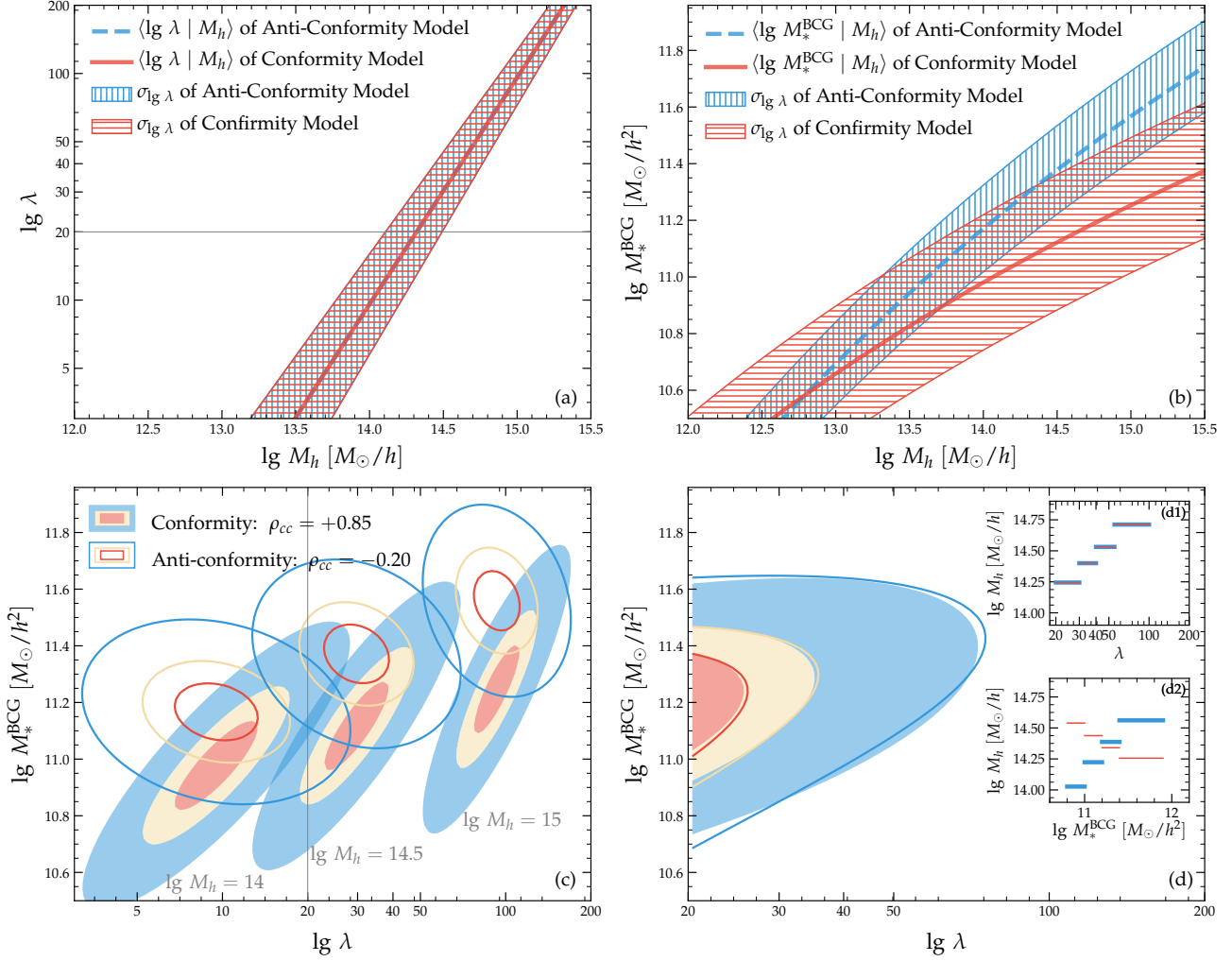


Figure 1. Pedagogical illustration of the degeneracy between conformity ($\rho_{cc} > 0$; red solid curves and filled contours) vs. anti-conformity ($\rho_{cc} < 0$; blue dashed curves and open contours) models of clusters. Panel (a): the mass–richness relations of the two models are exactly the same by design. Panel (b): the stellar-to-halo mass relations of the two models are different, with the conformity model having a shallower slope and larger scatter than the anti-conformity model. Panel (c): The three consecutive contours of each model indicate the 2D PDFs of clusters on the M_*^{BCG} vs. λ plane predicted at fixed log-halo masses of 14, 14.5, and 15 (from left to right), respectively. The differences are not observable due to the lack of individual halo mass measurements. Panel (d): The 2D abundance of clusters on the observed M_*^{BCG} vs. λ plane, predicted by the conformity (filled) and anti-conformity (open) models. The inset panels (d1) and (d2) show the average halo mass of clusters in four bins of λ and M_*^{BCG} , respectively. In each inset panel, thick blue and thin red lines indicate the predictions by the anti-conformity and conformity models, respectively. The two sets of model predictions are almost indistinguishable in their 2D abundances (panel d) and halo mass in bins of λ (panel d1), despite the large discrepancies shown in panels (b) and (c). This strong degeneracy can be potentially broken by measuring the halo mass of clusters in bins of M_*^{BCG} (panel d2).

with horizontally hatched band) has a shallower slope but a larger scatter than that of the anti-conformity model (blue dashed line with vertically hatched band). As a result, the two models will predict different average halo masses for clusters selected by the BCG stellar mass (as shown in Panel d2).

In the bottom left panel of Figure 1, filled and open contours indicate the 2D PDFs of M_*^{BCG} and λ at three fixed halo masses of $\lg M_h = 14, 14.5,$ and $15,$ of the conformity ($\rho_{cc} = 0.85$) and anti-conformity ($\rho_{cc} = -0.2$) models, respectively. Each contour has three levels at 20% (red), 50% (beige), and 90% (blue) enclosed probabilities expanding outwards. Unsurprisingly, the two models yield two drastically different $p(\ln M_*^{\text{BCG}}, \ln \lambda | M_h)$ at every mass. Yet, the 2D abundance of clusters on the M_*^{BCG} vs. λ diagram (bottom right panel) predicted by the two models are strikingly similar — the

filled (conformity) and open (anti-conformity) contours are mostly aligned and overlapping, leaving little observational signature to distinguish the two models from 2D abundance alone. In the two inset panels, we show the average halo mass of clusters in bins of λ (panel d1) and M_*^{BCG} (panel d2), respectively. As expected, the halo masses are exactly the same when binned by λ , as a result of the RHMRs being the same. Therefore, if we constrain conformity using just the 2D abundance and halo mass in bins of λ , there would be a strong degeneracy between the conformity and anti-conformity models, as will be demonstrated later in §4.1.

However, the two sets of predicted halo mass in bins of M_*^{BCG} are significantly different. The conformity model predicts that the average halo mass is a decreasing function of M_*^{BCG} , while the anti-conformity model predicts an increasing trend with M_*^{BCG} . This dis-

crepancy is likely related to the ‘‘halo mass equality’’ conundrum discovered in [Paper I](#), showing that the halo mass trend with M_*^{BCG} could be highly non-trivial and depends critically on the level of conformity within the cluster sample. More important, the strong discrepancy shown in the panel *d2* of [Figure 1](#) implies that the halo mass measurements for the low and high- M_*^{BCG} subsamples from [Paper I](#) could be the key in breaking the degeneracy between the two types of conformity models, as will be shown later in [§4.4](#). Note that the predictions of halo mass as a function of stellar mass shown in panel *d2* (and throughout this paper) are for central galaxies of clusters with $\lambda \geq 20$, therefore cannot be directly compared with the measurements for central galaxies of *all* haloes ([Mandelbaum et al. 2016; Zu & Mandelbaum 2016](#)).

4.2 Likelihood Model

To summarise our model parameters θ from [§3](#), we have in total 12 free parameters, including $\{A, \alpha, \sigma_{\ln \lambda, 0}, q\}$ for describing the RHMR, $M_{h,1}, \{M_{*,0}, \beta, \delta, \gamma, \sigma_{\ln M_*^{\text{BCG}} | M_h}\}$ for describing the SHMR, and $\{\rho_{cc,0}, s\}$ for describing the sign and level of the BCG-satellite conformity.

Since β and γ describe the low-to-intermediate mass portion of the SHMR, which is largely irrelevant to our constraint in the cluster mass regime, we apply two Gaussian priors informed by the constraint from [Zu & Mandelbaum \(2015\)](#) using the galaxy clustering and galaxy-galaxy lensing measurements from SDSS: $\beta \sim \mathcal{N}(0.33, 0.18^2)$ and $\gamma \sim \mathcal{N}(1.21, 0.19^2)$, respectively. For the rest of the parameters, we assume uniform priors so that each parameter could vary freely within a range that is much larger than potentially allowed by the data.

To recap our data vector from [§2](#), we have measured the total number of observed clusters N_{cls} , the BCG stellar mass and satellite richness of individual clusters $\{M_*^{\text{BCG}}, \lambda\}_{i=1 \dots N_{\text{cls}}}$, and the average halo mass of clusters binned in richness $\{M_h | [\lambda_{\min}^j, \lambda_{\max}^j]\}_{j=1 \dots 4}$. We will describe the likelihood model for each of the three components in turn below.

We assume a Poisson likelihood model for N_{cls} ,

$$\ln \mathcal{L}_{\text{Pois}} = N_{\text{cls}} \ln \langle N \rangle - \langle N \rangle - \ln \Gamma(N_{\text{cls}} + 1), \quad (17)$$

where $\langle N \rangle$ is the expected total number of clusters predicted by [Equation 14](#) and Γ is the Gamma function. For the 2D cluster abundance, we simply multiply all the individual $p(\ln M_*^{\text{BCG}}, \ln \lambda)$ so that

$$\ln \mathcal{L}_{\text{Indi}} = \sum_{i=1}^{N_{\text{cls}}} \ln p(\ln M_{*,i}^{\text{BCG}}, \ln \lambda_i), \quad (18)$$

where $p(\ln M_{*,i}^{\text{BCG}}, \ln \lambda_i)$ is the observing probability of cluster i derived from [Equation 10](#). For the halo mass in bins of richness, we assume a Gaussian likelihood model

$$\ln \mathcal{L}_{\text{Gaus}} = -\frac{1}{2} \ln |\mathbf{C}| - \frac{1}{2} (\mathbf{x} - \bar{\mathbf{x}})^T \mathbf{C}^{-1} (\mathbf{x} - \bar{\mathbf{x}}), \quad (19)$$

where the \mathbf{x} is the halo mass measurements for clusters in four richness bins from [Table 1](#), $\bar{\mathbf{x}}$ is the predicted average halo masses from [Equation 16](#), and \mathbf{C} is the error matrix associated with the halo mass measurements.

Finally, the full likelihood is the product of the three components

$$p(\mathbf{y} | \theta) = \mathcal{L}_{\text{Pois}} \times \mathcal{L}_{\text{Indi}} \times \mathcal{L}_{\text{Gaus}}, \quad (20)$$

and the posterior probability is proportional to the product of the likelihood and the prior probability $p(\theta)$

$$p(\theta | \mathbf{y}) \propto p(\mathbf{y} | \theta) p(\theta). \quad (21)$$

Table 2. Posterior constraints of the model parameters for the two models. The uncertainties are the 68% confidence regions derived from the 1D posterior probability distributions.

Parameters	Conformity Model	Anti-conformity Model
A	$3.44^{+0.03}_{-0.03}$	$3.41^{+0.03}_{-0.03}$
α	$1.06^{+0.03}_{-0.03}$	$0.96^{+0.03}_{-0.02}$
$\ln M_{h,1}$	$21.83^{+2.60}_{-2.18}$	$22.82^{+1.97}_{-2.10}$
$\ln M_{*,0}$	$20.57^{+1.20}_{-1.13}$	$20.23^{+1.31}_{-1.36}$
β	$0.35^{+0.18}_{-0.15}$	$0.42^{+0.18}_{-0.17}$
δ	$0.30^{+0.05}_{-0.04}$	$0.24^{+0.03}_{-0.03}$
γ	$1.21^{+0.19}_{-0.19}$	$1.20^{+0.20}_{-0.19}$
$\sigma_{\ln \lambda, 0}$	$0.32^{+0.03}_{-0.04}$	$0.39^{+0.03}_{-0.03}$
q	$-0.20^{+0.02}_{-0.03}$	$-0.13^{+0.01}_{-0.02}$
$\sigma_{\ln M_*}$	$0.40^{+0.09}_{-0.10}$	$0.28^{+0.10}_{-0.09}$
$\rho_{cc,0}$	$0.60^{+0.17}_{-0.23}$	$-0.48^{+0.24}_{-0.22}$
s	$0.08^{+0.05}_{-0.06}$	$-0.12^{+0.06}_{-0.05}$

4.3 Parameter Constraint

Equipped with the full likelihood model, we now set out to infer the joint posterior distribution of the 12 model parameters. We first perform the analysis by allowing $\rho_{cc,0}$ to vary freely between -1 and 1 , yielding a dominant solution that prefers a positive $\rho_{cc,0}$ (i.e., conformity), as well as a secondary solution with $\rho_{cc,0} < 0$ (i.e., anti-conformity). This model degeneracy is expected from our simple experiment in [§4.1](#). To thoroughly explore the two solutions separately, we then repeat our inference twice by first limiting $\rho_{cc,0} \in [0, 1)$ and then $\rho_{cc,0} \in (-1, 0]$ when sampling the posterior distributions, yielding a best-fitting conformity and an anti-conformity model, respectively. Since we will be distinguishing the two degenerate solutions using the weak lensing of clusters binned by M_*^{BCG} in [§4.4](#), we present the two solutions in parallel below without comparing their relative statistical significance.

For each inference, we employ the affine invariant Markov Chain Monte Carlo (MCMC) ensemble sampler [emcee \(Foreman-Mackey et al. 2013\)](#). We run the MCMC sampler for 2,000,000 steps for each analysis to ensure its convergence, and derive the posterior constraints after a burn-in period of 500,000 steps. The median values and the 68 per cent confidence limits of the 1D posterior constraints are listed in [Table 2](#).

[Figure 2](#) compares the two separate parameter constraints derived for the conformity (red) and anti-conformity (blue) models. For each model, the histograms in the diagonal panels show the 1D marginalised posterior distributions of each of the 12 parameters, and the contours in the off-diagonal panels are the 50% and 90% confidence regions for each of the parameter pairs. The gray solid line running through the $\rho_{cc,0}$ -related panels divides the conformity vs. anti-conformity models at $\rho_{cc,0} = 0$. In the top right corners, we provide a brief description of the functionality of each model parameter within each of the three components of our $p(\ln M_*^{\text{BCG}}, \ln \lambda | M_h)$ model (i.e., RHMR, SHMR, and BCG-satellite conformity).

[Figure 3](#) compares the predictions from the conformity (red) and anti-conformity (blue) posterior mean models to the data. The orange dots in the left panel represent the observed cluster distribution on the M_*^{BCG} vs. λ diagram, with the three thick gray dashed contour lines enclosing 20, 50, and 90 percentiles of the cluster sample (from the inside out), respectively. Red solid and blue dashed contour lines indicate the same three levels in percentiles predicted by the conformity

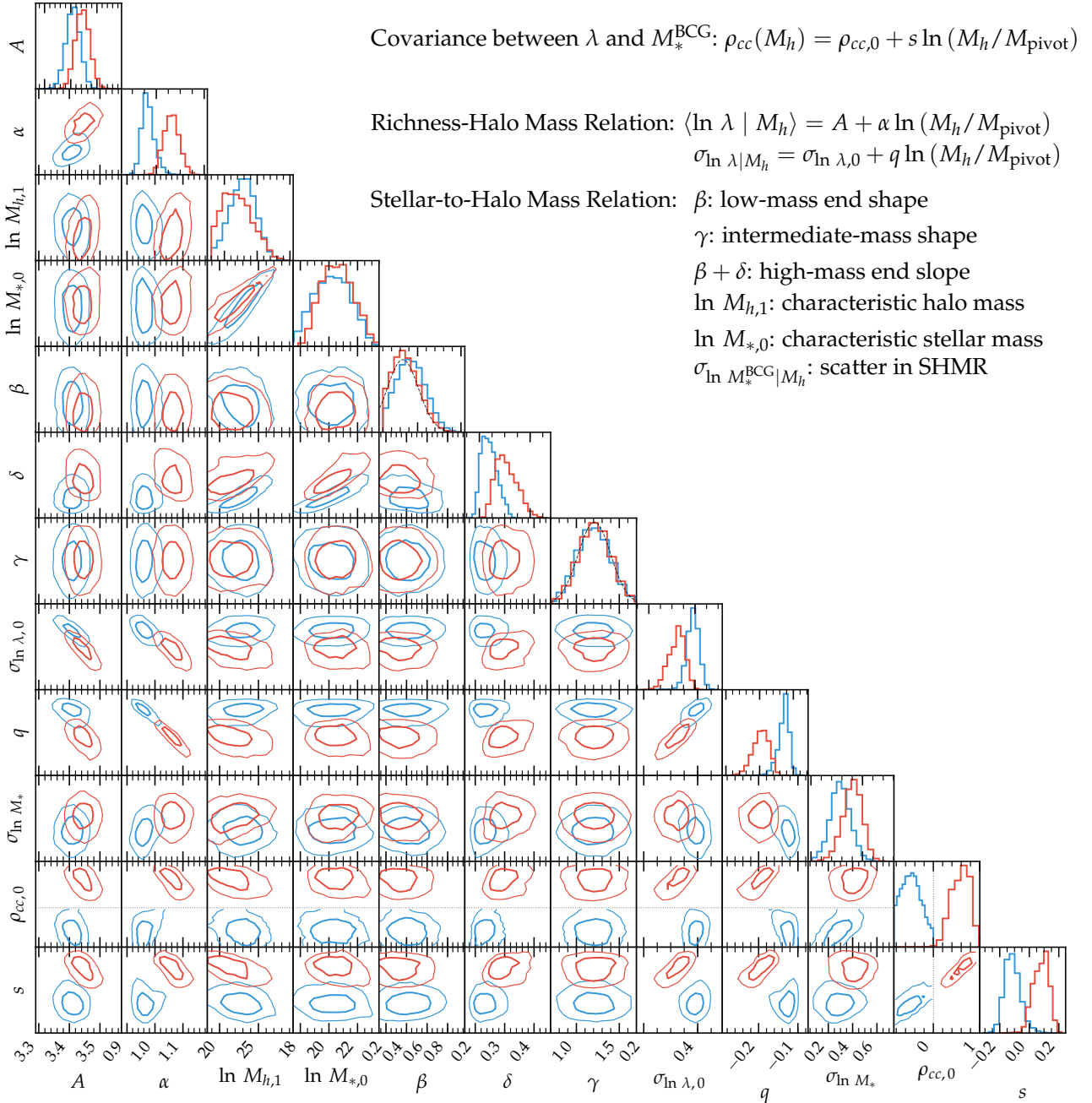


Figure 2. Parameter constraints of the conformity (red) and anti-conformity (blue) models. Diagonal panels show the 1D posterior distributions of each of the 12 parameters, while the off-diagonal panels indicate the 2D confidence regions (50 and 90 per cent from inside out) of the constraint on each of the parameter pairs. Gray dashed curves in the diagonal panels of β and γ are the Gaussian prior distributions. A short description of each parameter is given by the legend in the top right corner.

and anti-conformity posterior mean models. Both models provide adequate descriptions of the underlying 2D distributions of clusters on the M_*^{BCG} vs. λ diagram. The right panel of Figure 3 compares the weak lensing-measured halo masses in four bins of richness (open circles with errorbars) to those predicted by the conformity (red triangles) and anti-conformity (blue inverted triangles) posterior mean models. Both model predictions are in good agreement with the weak lensing mass measurements, with the (anti-)conformity model predictions slightly lower (higher) than the observations at the low rich-

ness end. Overall, Figure 3 confirms our expectation from Figure 1 that there exists a model degeneracy that cannot be overcome by the combination of 2D cluster abundance and halo mass measurements in bins of richness.

Figure 4 provides a more visually-appealing way of comparing the two model constraints. Instead of showing the posterior distributions of the 12 individual parameters, we examine the behaviors of the best-fitting RHRs (left), BCG-satellite conformities (middle), and SHMRs (right), respectively. In the left panel, we also show the

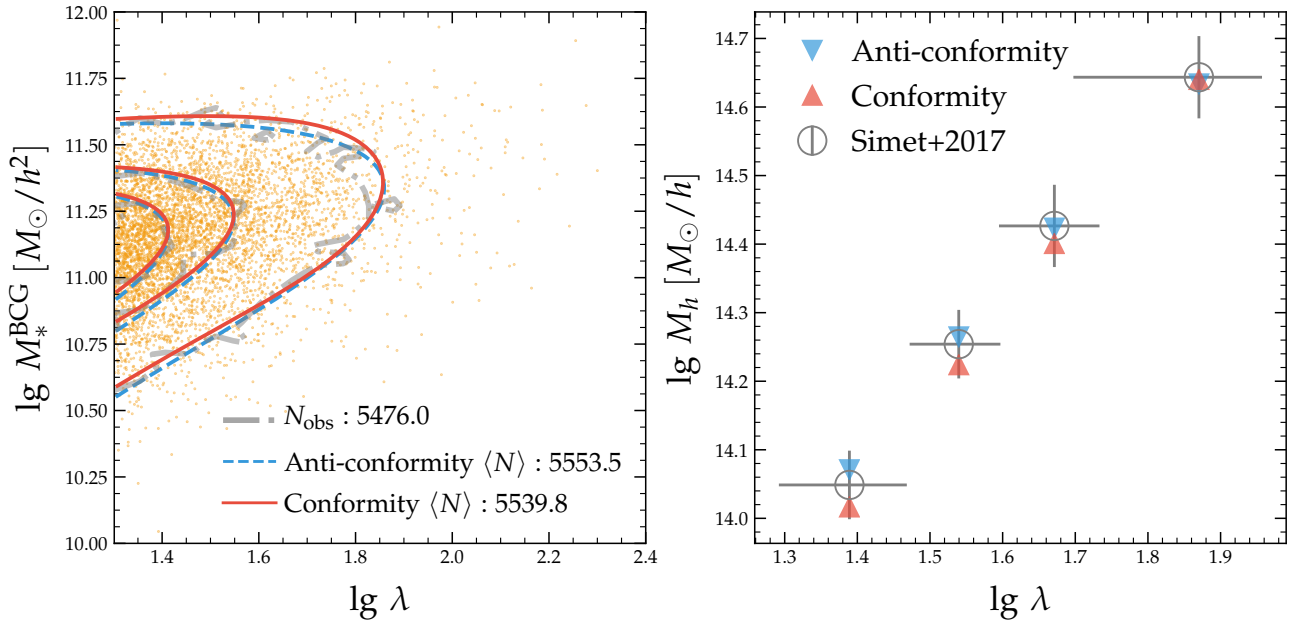


Figure 3. Comparison between the data and the predictions from the posterior mean parameters of the conformity (red solid) and anti-conformity (blue dashed) model constraints. *Left:* 2D PDFs of clusters on the M_*^{BCG} and λ plane. Gray dot-dashed contours and yellow points indicate the observed PDFs and individual clusters, respectively. The total number of observed and predicted clusters are marked by the legend in the bottom right. *Right:* average log-halo mass in four bins of richness. Open circles with errorbars are the measurements from Simet et al. (2017), and red and blue triangles indicate the posterior mean predictions from the conformity and anti-conformity models, respectively. Both models provide good fits to the data.

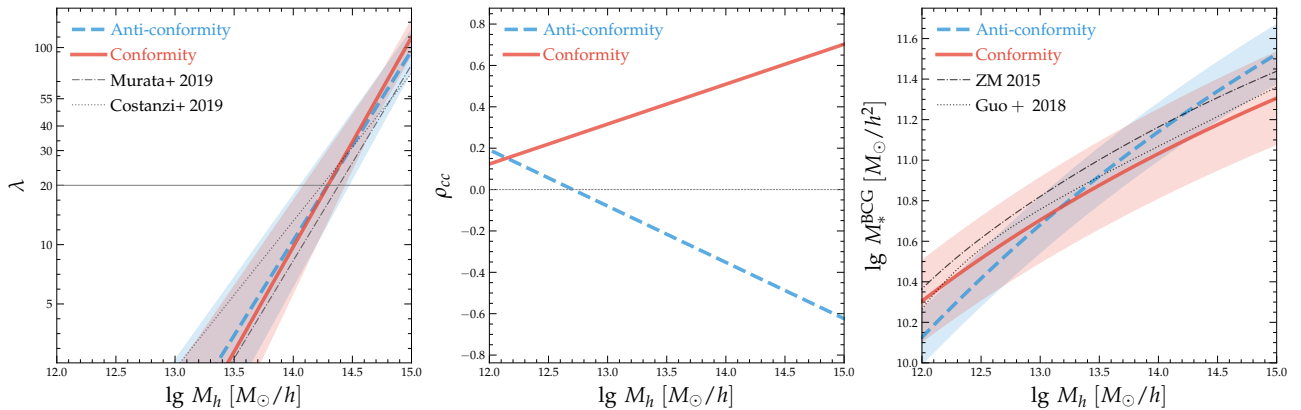


Figure 4. Mass–richness relation (left), correlation coefficient variation (middle), and stellar-to-halo mass relation (right), predicted by the conformity (red solid) and anti-conformity (blue dashed) posterior mean models. Dotted and dot-dashed lines in the left panel indicate the best-fitting models from Costanzi et al. (2019b) and Murata et al. (2018), respectively. In the right panel, dotted and dot-dashed curves are the best-fitting models from Guo et al. (2018) and Zu & Mandelbaum (2015), respectively. Shaded bands in the left and right panels indicate the $1-\sigma$ logarithmic scatter about the median scaling relations.

mean RHMRs derived by Murata et al. (2018) (gray dot dashed) and Costanzi et al. (2019b) (gray dotted) for the SDSS redMaPPer clusters. Unsurprisingly, the RHMRs predicted by the conformity (red solid) and anti-conformity (blue dashed) models are reasonably similar at $\lambda \geq 20$, because they are primarily constrained by the observed abundance and average halo mass of clusters binned in richness, which are independent of $\rho_{cc}(M_h)$. The shaded band about each mean RHMR indicates the dependence of scatter on halo mass. Compared to the Murata et al. (2018) result, our RHMRs have a higher amplitude but the same slope, likely due to a slight shift in the weak lensing halo mass calibration compared to ours — they used

the shear catalogue from the HSC survey and a cluster sample with $z \in [0.1, 0.33]$. The RHMR derived by Costanzi et al. (2019b) has a much shallower slope than the other three, because they also varied cosmology while inferring the RHMR.

In the right panel of Figure 4, we compare the SHMRs inferred from the conformity (red solid) and anti-conformity (blue dashed) models, as well as the results from Zu & Mandelbaum (2015) (gray dot-dashed) using the galaxy clustering and galaxy–galaxy lensing at $z \sim 0.1$ and from Guo et al. (2018) (gray dotted) using the LOWZ galaxy clustering at the same redshift of our sample. Unlike the RHMRs, our two inferred SHMRs are significantly different, with

the conformity SHMR showing a shallower slope but a larger scatter than the anti-conformity one. Additionally, the result from Guo et al. (2018) is consistent with the conformity constraint, while the Zu & Mandelbaum (2015) curve has a similar slope but a higher amplitude compared to the conformity prediction, probably due to some redshift evolution of the SHMR from $z \sim 0.25$ to 0.1. Both the Guo et al. (2018) and Zu & Mandelbaum (2015) constraints are strongly inconsistent with the prediction by the anti-conformity model.

Finally, the middle panel of Figure 4 shows the correlation coefficients as functions of halo mass $\rho_{cc}(M_h)$, predicted by the conformity (red solid) and anti-conformity (blue dashed) models, respectively. Interestingly, both predictions favor a weak correlation between the BCG stellar mass and satellite richness at the low mass end (i.e., below $10^{13} h^{-1} M_\odot$), but bifurcate into strong positive and negative correlations at the high mass end (i.e., above a few times $10^{14} h^{-1} M_\odot$). The two different scenarios point to drastically different paths of galaxy formation within massive clusters — the conformity model implies a *correlated* growth between the BCG and satellite galaxies, while the anti-conformity model favors a *compensated* growth between the two galaxy populations. Therefore, it is vital to observationally distinguish the two scenarios for a better understanding of the underlying physics behind cluster galaxy formation.

4.4 Resolving the “Halo Mass Equality” Conundrum

As mentioned in the introduction, we are hopeful that the existence of a strong (anti-)conformity between the BCG stellar mass and satellite richness could potentially reconcile the “halo mass equality” conundrum — that is, when split into two halves by the median M_*^{BCG} at fixed λ , the two cluster subsamples have almost the same average halo mass, despite having a 0.34 dex discrepancy in their average M_*^{BCG} . We refer readers to Paper I for details on the subsample definition (see also Figure 5) and the original “halo mass equality” conundrum. We now explore whether one of the two posterior mean models we inferred in §4.3 is consistent with such “halo mass equality” phenomenon.

Figure 5 illustrates the differences between the anti-conformity (top row) and conformity (bottom row) models in decomposing the underlying halo mass distribution of the high and low- M_*^{BCG} subsamples. In each row, the left panel shows the variation of the average halo mass across the M_*^{BCG} vs. λ plane, with the logarithmic mass indicated by the colourbar in the bottom right. The gray dashed line represents the median $M_*^{\text{BCG}}-\lambda$ relation that splits the clusters into high and low- M_*^{BCG} subsamples in Paper I. Interestingly, the high- M_*^{BCG} clusters have on average higher halo masses than the low- M_*^{BCG} systems in the anti-conformity scenario (top left), while the trend of average halo mass with M_*^{BCG} is less clear in the conformity model (bottom left). We further clarify the halo mass trend with M_*^{BCG} in the middle panels, by showing the average log-halo mass as functions of M_*^{BCG} at four different richnesses of 20 (purple), 30 (green), 50 (yellow), and 100 (red), respectively. Clearly, all the four curves are monotonic with M_*^{BCG} in the anti-conformity model, but exhibit a plateau above $M_*^{\text{BCG}} \sim 10^{11} h^{-2} M_\odot$ in the conformity model. Note that the plateau is a unique feature predicted by the conformity, and cannot be mimicked by systematic effects like the mis-centring, which primarily affects the low- M_*^{BCG} systems.

The right panels of Figure 5 provide the key to potentially resolving the “halo mass equality” conundrum. In each panel, we show the underlying halo mass distributions for all (gray dotted), low- M_*^{BCG} (blue dashed), and high- M_*^{BCG} (red solid) clusters, respectively. Addition-

ally, we indicate the average weak lensing halo mass ($\langle M_h^{2/3} \rangle^{3/2}$; see Mandelbaum et al. 2016) of each of the three distributions using a short vertical line of the same colour at the bottom. Unsurprisingly, the two subsamples are predicted to have a ~ 0.3 dex discrepancy in their average weak lensing halo mass in the anti-conformity model (top right), due to the monotonic trend of halo mass with M_*^{BCG} across the entire richness range.

However, in the bottom right panel of Figure 5, the conformity model predictions exhibit exactly the same “halo equality” as discovered in Paper I — the two subsamples of clusters have almost the same weak lensing halo mass, despite the significant difference in the shape of their halo mass distributions. In particular, the conformity model predicts a stronger low- M_h tail and a more massive peak for the halo mass distribution of the low- M_*^{BCG} subsample than the high- M_*^{BCG} one. More important, the low- M_h tail and the high- M_h peak somehow conspire to produce an average weak lensing halo mass that is very similar to that of the high- M_*^{BCG} clusters, thereby resolving the “halo mass equality” conundrum of Paper I.

The average halo mass estimated by Paper I for the low and high- M_*^{BCG} subsamples is $\lg M_h = 14.24 \pm 0.02$, roughly 10% lower than predicted by the best-fitting conformity model (14.28). However, as mentioned in §2.2, the estimated uncertainty of halo mass (± 0.02 dex) in Paper I does not include many of the systematic uncertainties that were included by Simet et al. (2017), therefore should be considered a lower limit. If we assume the typical mass error of 0.05 dex from Simet et al. (2017), e.g., by adding an extra 0.03 dex of fully-correlated systematic error, the two sets of halo mass estimates would be consistent within 1σ . In the future, we can further tighten the constraints on conformity by applying a uniform halo mass measurement method to clusters binned by M_*^{BCG} and λ .

Before moving on to the second half of the paper, we summarise our key results so far as follows.

- We have inferred the best-fitting models under different assumptions of conformity vs. anti-conformity between the BCG stellar mass and satellite richness, using the combination of cluster abundance and weak lensing mass of clusters binned in λ as constraints.
- Both best-fitting conformity and anti-conformity models provide good descriptions of the data, but they predict significantly different average halo masses for clusters binned in M_*^{BCG} .
- By comparing to the weak lensing halo mass measurements of the low and high- M_*^{BCG} clusters, we demonstrated that while the anti-conformity model is strongly disfavored by the data, the best-fitting conformity model predicts the same average halo mass for the two cluster subsamples, thereby resolving the “halo mass equality” conundrum discovered by Paper I (Figure 5).

5 MODELLING CLUSTER WEAK LENSING WITH CONFORMITY AND ASSEMBLY BIAS

Apart from the “halo mass equality” conundrum that we focused on in the first part of this paper, Paper I also discovered that the low- M_*^{BCG} clusters on average exhibit a 20% lower concentration (5.87 vs. 6.95) and a $\sim 10\%$ higher large scale bias than their low- M_*^{BCG} counterparts. Paper I suggested that the bias discrepancy could be an evidence of cluster assembly bias (Zu et al. 2017). However, while the concentration measurements from the small-scale weak lensing profiles are robust (modulo the degeneracy with the cluster mis-centring effect), the modelling of large-scale biases in Paper I is lacking, due to the omission of the halo assembly bias effect that governs the concentration–bias relation of clusters at fixed M_h .

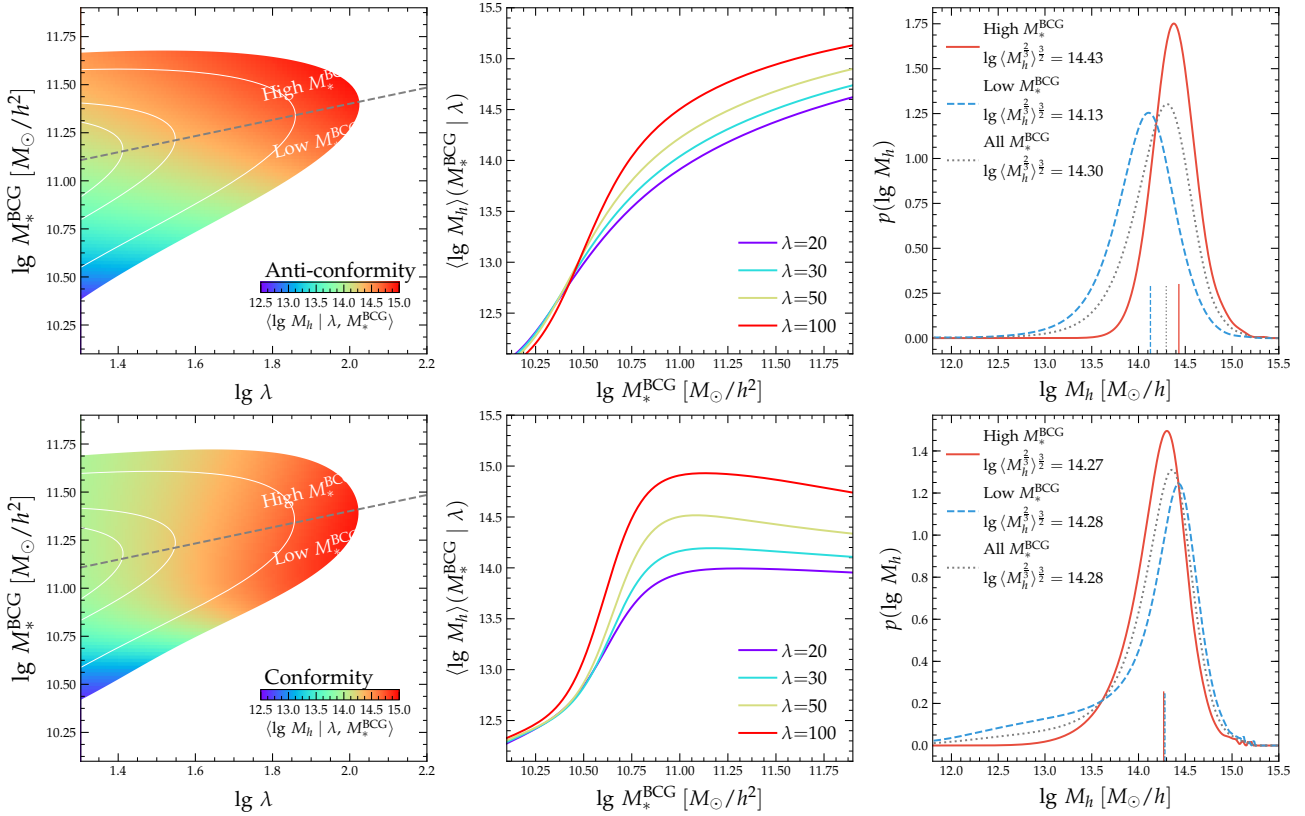


Figure 5. Predictions of halo mass distributions by the anti-conformity (top row) and conformity (bottom row) posterior mean models. In each row, the left panel shows the map of average log-halo mass on the M_*^{BCG} vs. λ plane, colour-coded by the horizontal colourbar in the bottom right corner. Gray dashed line indicates the median $\log\text{-}M_*^{\text{BCG}}$ vs. λ relation, which divides the clusters into two subsamples of high and low M_*^{BCG} with the same distribution of λ . The middle panel shows the variation of $\log\text{-}M_h$ as a function of M_*^{BCG} , at four fixed values of λ of 20 (purple), 30 (cyan), 50 (yellow), and 100 (red), respectively. The right panel compares the PDFs of $\log\text{-}M_h$ of the high- M_*^{BCG} (red solid) and low- M_*^{BCG} (blue dashed) subsamples, as defined in the left panel, with the PDF of all the clusters shown by the gray dotted curve. The predicted average weak lensing halo mass of each cluster (sub)sample is marked by the bottom vertical tick of the respective line color/style and shown in the legend. The two models predict significantly different halo masses for the high and low- M_*^{BCG} subsamples, despite reproducing the similar observables in Figure 3.

Therefore, in the second part of this paper we will implement halo assembly bias in our posterior mean conformity model inferred from §4.3, in order to provide a more accurate model for the weak lensing profiles $\Delta\Sigma$ which can then be compared with the measurements for the low and high- M_*^{BCG} subsamples from Paper I.

To avoid distracting the impatient, we will directly present the $\Delta\Sigma$ predictions from our best-fitting analytic models that include the halo assembly bias and (anti-)conformity in this section. For those who are interested in the modelling details, we describe the calibration and prescription of halo assembly bias in Appendix §A, and the analytic model of weak lensing profiles in Appendix §B.

5.1 Fitting to Weak Lensing of High and Low- M_*^{BCG} Clusters

Figure 6 compares the stacked weak lensing measurements to those predicted by the posterior mean anti-conformity model (left column), conformity model without assembly bias (middle column), and conformity model with assembly bias (right column), respectively. The top and bottom rows are the same except for the labels of the y-axes ($\Delta\Sigma$ vs. $r_p\Delta\Sigma$). In each panel, red circles and blue squares are the weak lensing measurements of the high and low- M_*^{BCG} subsamples (same as those shown in the Figure 5 of Paper I), respectively, while red solid and blue dashed curves are the respective model pre-

dictions. The values of average concentration $\langle c \rangle$ and average bias $\langle b \rangle$ adopted by each model are indicated in the top right of each top panel. Unsurprisingly, the predictions by the anti-conformity model in the left panels fail to describe the $\Delta\Sigma$ measurements on all scales, due to the factor of two difference between the two predicted average halo masses and the $\sim 30\%$ discrepancy between the two predicted biases.

In the middle panels of Figure 6, the conformity-only (i.e., without assembly bias) model provides good description of the small-scale $\Delta\Sigma$ measurements, echoing the finding in Figure 5 that the average weak lensing halo masses of the two subsamples are similar. On large scales, the two predicted $\Delta\Sigma$ profiles converge to the same amplitudes, because the similar average halo masses produce similar biases in the absence of assembly bias. In the right panels of Figure 6, the small-scale behavior of the $\Delta\Sigma$ profiles predicted by the conformity+AB (i.e., with assembly bias) model are the same as in the middle panels, but on large scales the two predicted curves differ by about 10% — the high- M_*^{BCG} clusters are more concentrated, producing a lower bias than the low- M_*^{BCG} systems due to the cluster assembly bias effect.

Due to the relatively large errorbars of $\Delta\Sigma$ on large scales, it is difficult to ascertain whether the conformity+AB model is superior to the conformity-only model. Therefore, we further examine the large-

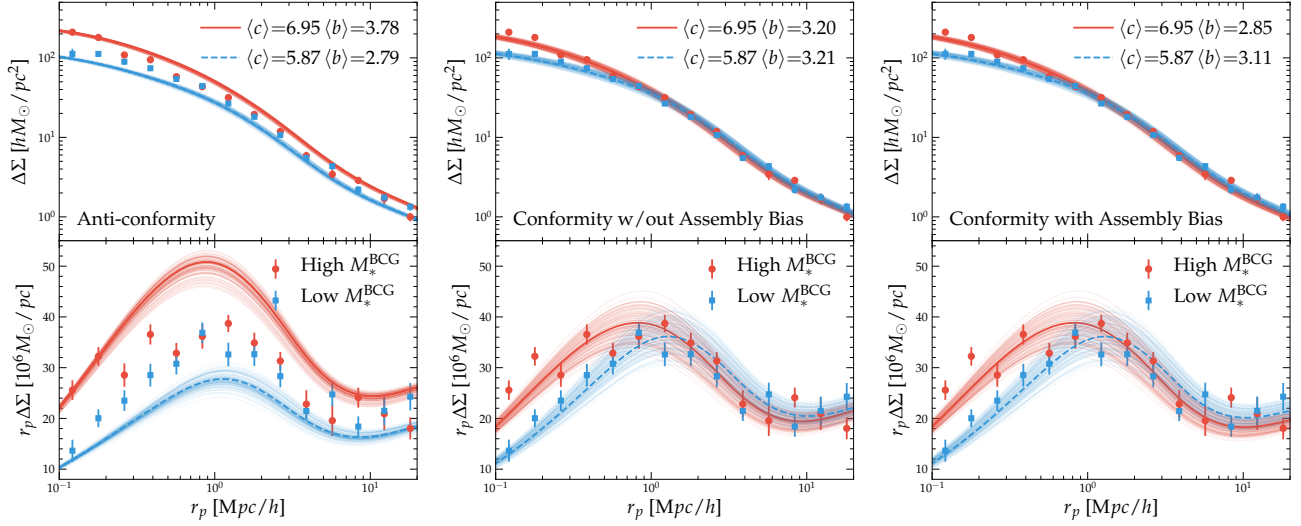


Figure 6. Comparison between the surface density contrast profile $\Delta\Sigma$ measured by Paper I from weak lensing and that predicted by three different models: anti-conformity (left column), conformity without assembly bias (middle column), and conformity with assembly bias (right column). In each column, the top and bottom panels show the same information except that the y-axis of the bottom panel is $r_p\Delta\Sigma$. In each panel, red circles and blue squares with errorbars are the weak lensing measurements for the high and low- M_*^{BCG} subsamples, respectively. Red solid and blue dashed thick curves are the predictions from the respective posterior mean model, while the bundle of thin curves around each thick curve is predicted from 100 random steps along the respective MCMC chain from Figure 2. The values of average concentration and bias adopted by each model are listed in the top right corner of each column. For the $\Delta\Sigma$ prediction, we adjust the average halo concentrations to be the best-fitting values inferred from Paper I on small scales, but predict the large-scale bias using different prescriptions (see text for details).

scale behaviors of the three models in Figure 7, where we show the projected cross-correlation functions between clusters and LOWZ galaxies (left) and the cluster galaxy number density profiles measured from the cross-correlations with photometric galaxies (right). Although we cannot directly measure the cluster biases directly from the cross-correlations with galaxies, which also depend on the bias of the galaxies (Xu et al. 2021), we can distinguish the three models by examining the ratio between the cross-correlations of the high and low- M_*^{BCG} with galaxies, which is a direct measure of b_+/b_- independent of galaxy bias.

In each panel of Figure 7, red and blue circles with errorbars indicate the measurements for the high and low- M_*^{BCG} subsamples, respectively. In the bottom sub-panel, red circles are the ratio between the measurements of the two subsamples. The gray shaded region in the left panel indicates the projected distances that are affected by the fibre collision in BOSS. Figure 7 is the same as the Figure 6 of Paper I, except that we mark the large-scale ratios predicted by the anti-conformity (dotted horizontal line), conformity-only (dot-dashed), and conformity+AB (solid) models in the bottom sub-panels. Clearly, the anti-conformity prediction is ruled out by the data. The conformity-only prediction without assembly bias is also disfavored by the observations, which exhibit a 10% bias discrepancy between the two subsamples. Meanwhile, the direction and amplitude of this bias discrepancy is in good agreement with the prediction by the conformity model with assembly bias. This is very reassuring — the combination of BCG-satellite conformity and cluster assembly bias not only predicts the correct weak lensing masses of clusters selected by M_*^{BCG} , therefore resolving the intriguing conundrum discovered in Paper I, but also accurately reproduces the large-scale bias inversion with M_*^{BCG} using the cluster assembly bias model directly predicted by the ΛCDM simulations.

5.2 Exploring Projection Effects

The projection effects in photometric cluster detection could induce systematic errors in the cluster observables that could sometimes masquerade as physical phenomena (Zu et al. 2017; Busch & White 2017). As mentioned in the introduction, To et al. (2020) discussed the possibility of projection effects to induce a positive correlation between BCG luminosity and richness, by enhancing the estimated richness in the dense environments that potentially host older and more luminous BCGs at fixed halo mass. If the projection effects are indeed the culprit, we should expect some correlation between the BCG stellar mass and the level of cluster membership contamination due to projection effects.

To investigate whether the strong conformity and assembly bias signals are partly induced by projection effects, we adopt the average membership distance R_{mem} as our measure of the projection effect in each cluster, defined as

$$R_{\text{mem}} = \frac{\sum_i (p_m^i R_i)}{\sum_i p_m^i}, \quad (22)$$

where p_m^i and R_i are the membership probability and the projected distance from the BCG of the i -th member galaxy candidate in that cluster, respectively. Miyatake et al. (2016) initially used R_{mem} as a proxy for halo concentration but found an extremely high signal of cluster assembly bias that is inconsistent with the ΛCDM simulations. Zu et al. (2017) later demonstrated that R_{mem} is strongly correlated with the fraction of spurious member galaxies in each cluster, causing the inconsistency between the Miyatake et al. (2016) measurement and ΛCDM . Therefore, we expect R_{mem} to be a good indicator of the level of membership contamination in individual clusters.

We first examine the distributions of the low and high- M_*^{BCG} clusters on the R_{mem} vs. λ plane, which is shown on the left panel of Figure 8. Red and blue contours indicate the 20%, 50%, and 90% en-

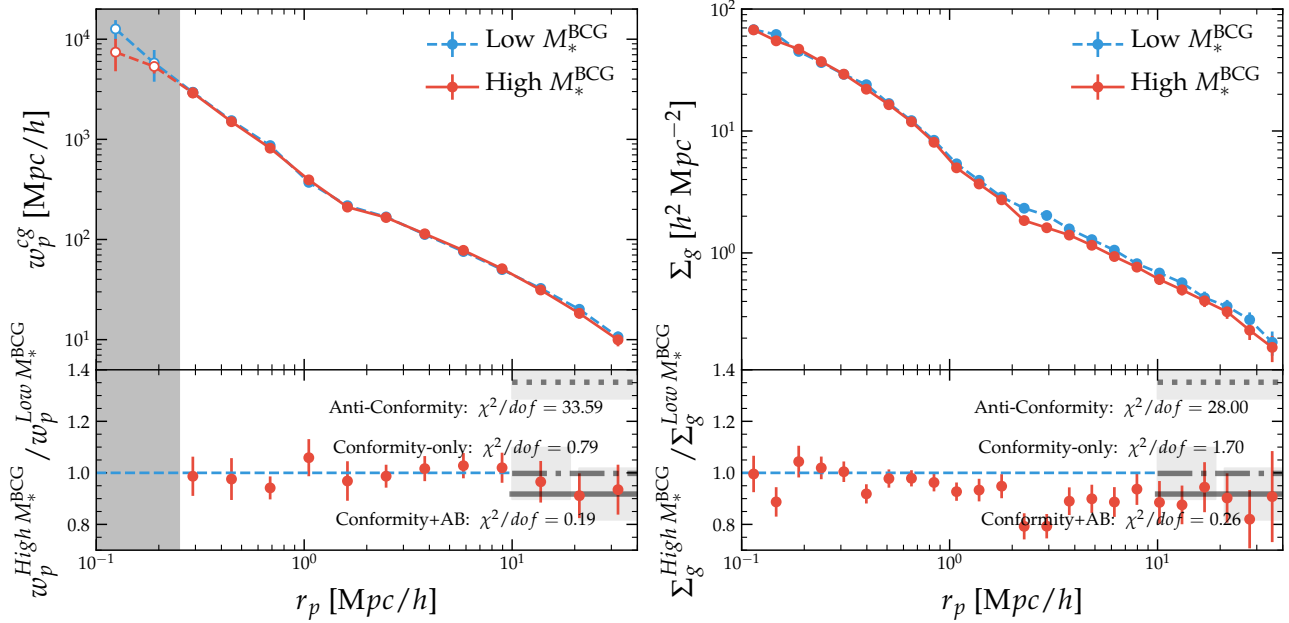


Figure 7. *Left panel:* Comparison of the projected correlation functions w_p^{CG} of the low (blue) and high (red) M_*^{BCG} subsamples with the BOSS LOWZ spectroscopic galaxy sample in the upper sub-panel, with the ratio of the two shown in the bottom sub-panel. The gray shaded region on the left indicates the distance scales that are affected by the fibre collision in BOSS. *Right panel:* Similar to the left panel, but for the excess galaxy surface number density profile Σ_g calculated from the SDSS DR8 imaging. In each sub-panel, the bias ratios predicted by the anti-conformity, conformity-only (i.e., without assembly bias), and conformity+AB (i.e., with assembly bias) models are indicated by the gray horizontal dotted, dot-dashed, and solid lines on scales above $10h^{-1}$ Mpc, respectively. The gray shaded band around each horizontal line indicates the 1σ uncertainty predicted by the constraints from Figure 2.

closed regions, while the red circles and blue squares with errorbars show the median R_{mem} as functions of λ for the high and low- M_*^{BCG} subsamples, respectively. The two sets of contours and median relations are well aligned, showing no systematic offset between the high and low- M_*^{BCG} subsamples in R_{mem} . The solid black line is a fit to the median relations that we use to divide each M_*^{BCG} -based subsample into low and high- R_{mem} quarter-samples for the test on the right panel.

The right panel of Figure 8 is similar to the left panel of Figure 7, except for that we divide each of the low and high- M_*^{BCG} subsamples in half based on the solid black line in the left panel and calculate the ratios between the high and low- M_*^{BCG} signals within each R_{mem} half in the bottom right panel. Filled and open red circles (blue squares) indicate the measurements for the high and low- R_{mem} quarter-samples split from the high (low)- M_*^{BCG} subsample, respectively. The high- R_{mem} profiles exhibit enhanced clustering on all scales above $400 h^{-1}$ kpc than the low- R_{mem} ones due to strong projection effects, echoing the findings in Sunayama et al. (2020). However, the amplitudes of the relative enhancement are the same between the low and high- M_*^{BCG} subsamples, indicating similar projection effects in the high- R_{mem} clusters regardless of the BCG stellar mass.

Despite the strong projection effects of the high- R_{mem} clusters, the ratio profiles in the bottom panels are both in good agreement with the prediction from the conformity+AB model as in Figure 7, though they are also consistent with the prediction from the conformity-only model due to the large uncertainties. Therefore, using the average radius of the member galaxy candidates R_{mem} as a proxy of the projection effect, we do not find any correlation between projection effect and BCG stellar mass that could induce the strong conformity we detected among the SDSS clusters, nor do we find any evidence

that our detected cluster assembly bias signal depends on the level of projection effects within the sample.

6 PHYSICAL IMPLICATIONS

6.1 Could Dry Mergers Drive the Strong BCG-Satellite Conformity?

The physical conformity between the BCG stellar mass and satellite richness implies a correlated growth between the BCGs and satellite galaxies inside clusters, and the increasing trend of ρ_{cc} with M_h suggests that the BCGs in the most massive haloes almost grow in lockstep with the accretion of satellite galaxies. This strong conformity could naturally occur if a significant fraction of the BCG stellar mass growth is *ex situ*, via the dry mergers with massive satellite galaxies that were transported to the cluster centre by dynamical friction (Chandrasekhar 1943; White 1976). Indeed, observations indicate that the mode of BCG stellar mass growth switched from *in situ* star formation to *ex situ* stellar accretion around $z \sim 1$ (Webb et al. 2015; McDonald et al. 2016; Vulcani et al. 2016; Lavoie et al. 2016; Groenewald et al. 2017; Zhao et al. 2017).

In order for dry mergers to drive a correlated scatter between BCG stellar mass and satellite richness, the merger-induced stellar growth should be significant, e.g., comparable with the intrinsic scatter in the cluster SHMR of ~ 0.05 – 0.1 dex (Golden-Marx et al. 2021). Observationally, the stellar growth from dry mergers since $z \sim 1$ varies between 30% (Collins et al. 2009; Bundy et al. 2017; Lin et al. 2017) and almost a factor of two (Whiley et al. 2008; Burke & Collins 2013; Lidman et al. 2013). However, semi-analytic models (SAMs) predict that the BCG stellar mass could grow by a factor of 3–4 between $z = 1$ and $z = 0$ (De Lucia & Blaizot 2007; Ruzkowski & Springel 2009;

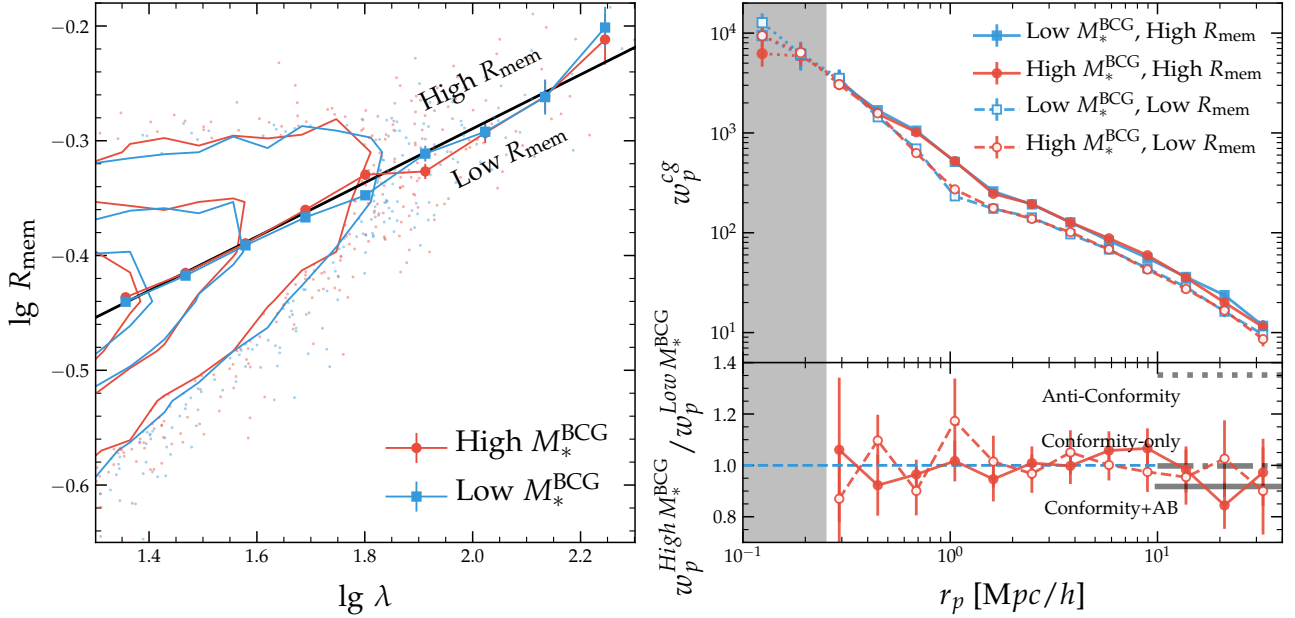


Figure 8. Impact of projection effects on the detection of conformity and assembly bias, using the average member galaxy distance R_{mem} as a proxy for the strength of projection effects. *Left:* Distributions of low (blue) and high (red) M_*^{BCG} clusters on the R_{mem} vs. λ plane. Each set of contour lines indicate the 20%, 50%, and 90% enclosed regions from the inside out. Red circles and blue squares show the median R_{mem} at fixed λ of the low and high- M_*^{BCG} subsamples, with the errorbars indicating the uncertainties on the median. The solid black line is a power-law fit to the two median relations, dividing the clusters into low and high- R_{mem} populations. *Right:* Similar to the left panel of Figure 7, but for subsamples further split by R_{mem} . We do not detect any significant dependence of M_*^{BCG} or bias ratio on R_{mem} .

Laporte et al. 2013; Oogi et al. 2016). The discrepancy between SAM predictions and observations is partly due to the numerical uncertainties in modelling dynamical friction (Jiang et al. 2008; Boylan-Kolchin et al. 2008), and it is also unclear what fraction of the accreted stars would end up in the diffuse intra-cluster light (Murante et al. 2007; Contini et al. 2018).

Alternatively, using a self-consistent model of the observed conditional stellar mass functions across cosmic time, Yang et al. (2013) carefully accounted for the total amount of *in situ* growth by modelling the star formation histories of central galaxies as a function of halo mass, stellar mass, and redshift. Their indirect method estimated that at $z \geq 2.5$ less than 1% of the stars in the progenitors of massive galaxies are formed *ex situ*, but this fraction increases rapidly with redshift, becoming $\sim 40\%$ at $z=0$. Therefore, by combining the observations, SAM predictions, and indirect estimates, we expect the average amount of merger-induced stellar mass growth to be between 0.1–0.3 dex, hence more than enough for driving a correlated scatter with richness.

Finally, the observed richness roughly corresponds to the number of massive, quenched satellite galaxies in each cluster, i.e., the same type of galaxies that would preferentially merge with the BCG within a Hubble time. For instance, Boylan-Kolchin et al. (2008) estimated that roughly 10–20% of all the accreted satellites with mass ratio above 1:10 would merge with the BCG within 7 Gyr due to dynamical friction (see also Jiang et al. 2008). As a result, the observed conformity between BCG stellar mass and richness could be strongly boosted by the fact that the low-mass, star-forming satellites are often not included when calculating the richness of optical clusters.

6.2 Is BCG-Satellite Conformity Consistent with the $c - M_*^{\text{BCG}}$ and $c - \lambda$ Relations?

Paper I showed that halo concentration is one of the key drivers of scatter in the SHMR of clusters, so that clusters with more concentrated cores host more massive BCGs at fixed halo mass — a positive $c - M_*^{\text{BCG}}$ correlation. In Paper I, we speculated that the correlation between c and M_*^{BCG} is caused by the fact that the *in situ* stellar mass growth of the BCGs is closely tied to the rapid growth of dark matter mass at early times. At the onset of cluster formation, fast accretion and frequent mergers not only built up the central cores of dark matter haloes (Zhao et al. 2003; Klypin et al. 2016), but also drove strong starbursts in the progenitors of the BCGs via rapid cooling flows and shocks, respectively (Fabian 1994; McDonald et al. 2012; Barnes & Hernquist 1991; Mihos & Hernquist 1996; Hopkins et al. 2013).

Meanwhile, there exists a well-known anti-correlation between the concentration and substructure abundance of haloes at fixed halo mass (Giocoli et al. 2010), which should translate to a $c - \lambda$ anti-correlation at fixed M_h . Combining this anti-correlation with the positive correlation between c and M_*^{BCG} , one might naively expect that the clusters with high λ (hence low c) would host less massive BCGs than their low- λ counterparts at fixed M_h — an anti-conformity between M_*^{BCG} and λ , in apparent contradiction with our finding of a strong BCG-satellite conformity from the data.

Before delving into the astrophysics in §6.3, the expectation of a BCG-satellite anti-conformity is a statistical fallacy, as correlations are non-transitive properties — the observed correlation between M_*^{BCG} and c , combined with the anti-correlation between c and λ , does not necessarily yield a negative correlation between M_*^{BCG} and λ . For the correlation matrix between the three quantities c , λ , and

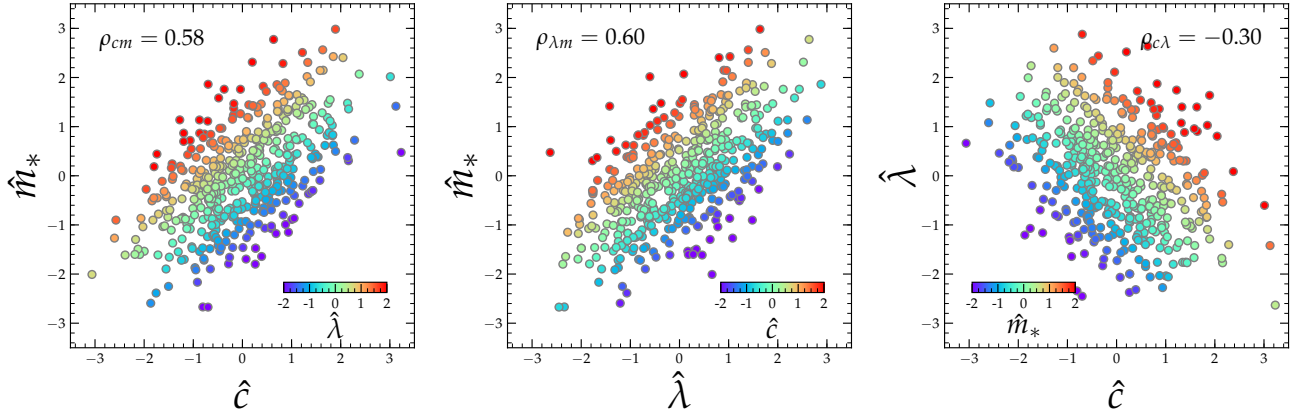


Figure 9. A toy model illustrating the relations between the relative BCG stellar mass \hat{m}_* , relative richness $\hat{\lambda}$, and relative concentration \hat{c} at fixed halo mass. The three panels show the distributions of 500 mock clusters generated with Equation 29 on the planes of $\hat{c}-\hat{m}_*$ (left), $\hat{\lambda}-\hat{m}_*$ (middle), and $\hat{c}-\hat{\lambda}$ (right), respectively. In each panel, each filled circle is colour-coded by the value of the third quantity (other than the quantities in the x and y axes) according to the inset colourbar. The Pearson cross-correlation coefficient is shown by the legend on the top left of each panel. Our toy model of Equation 29 successfully reproduces the observed correlation between concentration and BCG stellar mass (left), BCG-satellite conformity (middle), and the simulation-predicted anti-correlation between concentration and richness (right).

$$M_*^{\text{BCG}},$$

$$\mathbf{A} = \begin{pmatrix} 1 & \rho_{c\lambda} & \rho_{cm} \\ \rho_{c\lambda} & 1 & \rho_{\lambda m} \\ \rho_{cm} & \rho_{\lambda m} & 1 \end{pmatrix}, \quad (23)$$

where $\rho_{c\lambda}$, ρ_{cm} , and $\rho_{\lambda m}$ are the correlation coefficients between the three pairs of quantities indicated by the subscripts ($\rho_{\lambda m}$ is equivalent to our conformity parameter ρ_{cc} in §3). In order for \mathbf{A} to be positive-definite, the determinant shall be positive,

$$|\mathbf{A}| = 1 - \rho_{\lambda m}^2 - \rho_{c\lambda}^2 - \rho_{cm}^2 + 2\rho_{c\lambda}\rho_{\lambda m}\rho_{cm} > 0, \quad (24)$$

so that $\rho_{\lambda m}$ has to be in between

$$\rho_{c\lambda}\rho_{cm} \pm \sqrt{(1 - \rho_{c\lambda}^2)(1 - \rho_{cm}^2)}. \quad (25)$$

Assuming $\rho_{c\lambda} = -0.3$ and $\rho_{cm} = 0.5$, we obtain the statistically allowed range of $\rho_{\lambda m}$ as

$$-0.68 < \rho_{\lambda m} < 0.98, \quad (26)$$

i.e., the correlation between BCG stellar mass and satellite richness can be as strongly positive as possible given reasonable values of a negative $\rho_{c\lambda}$ and a positive ρ_{cm} . For $\rho_{\lambda m}$ to be strictly below zero when the signs of $\rho_{c\lambda}$ and ρ_{cm} are different, we need

$$\rho_{c\lambda}^2 + \rho_{cm}^2 > 1. \quad (27)$$

Therefore, for $\rho_{\lambda m}$ to be strictly negative when $\rho_{c\lambda} = -0.3$, the correlation between concentration and BCG stellar mass has to be greater than $\rho_{cm} = 0.95$ — a plausible value but quite unlikely in the presence of *ex situ* BCG growth.

6.3 A Toy Model for the $M_*^{\text{BCG}} - \lambda - c$ Relation at Fixed M_h

The key to understanding the connection between M_*^{BCG} , c , and λ at fixed M_h is to decompose the observed M_*^{BCG} into two components of different physical origins and formation epochs. As discussed in §6.1, the amount of *ex situ* BCG stellar mass is likely related to the frequency of late-time BCG-satellite mergers, which is directly tied to the number of massive quenched satellites, i.e., λ ; The *in situ* portion

of M_*^{BCG} is likely tied to c due to the co-evolution of BCGs and dark matter haloes in the early phase of cluster formation. Therefore, it is plausible that at fixed M_h , M_*^{BCG} is positively correlated with *both* c and λ , while c and λ are themselves anti-correlated.

To illustrate such a physical connection between M_*^{BCG} , c , and λ at fixed M_h , we can build a simple toy model for explaining the scatter in the BCG stellar mass using two separate components sourced by concentration and richness. To remove the halo mass dependence in the toy model, we choose to model the *relative* BCG stellar mass \hat{m}_* defined in Equation 8 using the *relative* concentration \hat{c} (Equation A1) and the *relative* richness (Equation 9).

In particular, we assume \hat{m}_* can be written as the sum of the *in situ* and *ex situ* components with no extra source of stochastic variance,

$$\hat{m}_* = \hat{m}_{*,\text{in}} + \hat{m}_{*,\text{ex}}, \quad (28)$$

where the two terms on the right-hand side can be described by two linear terms of \hat{c} and $\hat{\lambda}$, respectively,

$$\hat{m}_* = f_{\text{in}} \hat{c} + f_{\text{ex}} \hat{\lambda}, \quad (29)$$

where

$$f_{\text{in}}^2 + f_{\text{ex}}^2 + 2f_{\text{in}}f_{\text{ex}}\rho_{c\lambda} = 1. \quad (30)$$

The equality in Equation 30 is to ensure that \hat{m} also has a unit variance when both \hat{c} and $\hat{\lambda}$ are unit-variance Gaussians. Assuming a $\rho_{c\lambda}$ of -0.30 , we find $f_{\text{in}} = 0.84$ and $f_{\text{ex}} \approx 0.85$ so that the equality in Equation 30 is reached and the resultant $\rho_{\lambda m}$ is roughly the value we inferred at M_{pivot} , i.e., 0.60.

To produce a sample of mock clusters, we assume \hat{c} and $\hat{\lambda}$ jointly follow a zero-means, unit-variances bivariate Gaussian with a correlation coefficient of -0.30 , and then generate 500 random values of \hat{c} and $\hat{\lambda}$ from this anti-correlated 2D Gaussian. We then derive 500 values of \hat{m}_* using Equation 29.

Figure 9 shows the correlation for each of the three pairs of quantities: $\hat{c}-\hat{m}_*$ (left), $\hat{\lambda}-\hat{m}_*$ (middle), and $\hat{c}-\hat{\lambda}$ (right), respectively. In each panel, each filled circle represents a mock cluster on the plane of the paired quantities, colour-coded by the value of the third quantity, indicated by the horizontal inset colourbar. The Pearson cross-correlation coefficient is indicated by legend on the top

left. Similar to the observations, \hat{m}_* shows strong positive correlations with both \hat{c} and \hat{m} , with comparable correlation coefficients of 0.59 and 0.60, respectively, despite that \hat{c} and \hat{m} are by design negatively correlated. Therefore, such an extremely simple model of Equation 29 can qualitatively reproduce the two key observations in Paper I and in this paper, the BCG-concentration correlation (left) and the BCG-satellite conformity (middle), respectively, without breaking the concentration-richness anti-correlation robustly predicted by simulations (right). The success of this toy model is very encouraging, pointing at a viable path to building a more comprehensive model of $M_*^{\text{BCG}} - \lambda - c$ connection for future cluster surveys.

7 SUMMARY AND CONCLUSION

We have inferred the level of conformity within the SDSS redMaPPer clusters, defined as the correlation coefficient ρ_{cc} between the BCG stellar mass M_*^{BCG} and satellite richness λ at fixed halo mass, using the observed abundance and weak lensing of clusters as functions of both M_*^{BCG} and λ . With the richness-halo mass relation largely anchored by the weak lensing mass of clusters binned in richness

$$\langle \ln \lambda \mid M_h \rangle = 3.44 + 1.06 \ln \left(M_h / 3 \times 10^{14} \right), \quad (31)$$

our best-fitting conformity model with

$$\rho_{cc}(M_h) = 0.60 + 0.08 \ln \left(M_h / 3 \times 10^{14} \right) \quad (32)$$

can successfully resolve the “halo mass equality” conundrum discovered in Zu et al. (2021) — when split by M_*^{BCG} at fixed λ , the low and high- M_*^{BCG} clusters have the same average weak lensing halo mass, despite the 0.34 dex discrepancy in their average BCG stellar mass. Our method of reconstructing the interconnection between multiple cluster observables using the abundance and weak lensing of clusters can be naturally extended to X-ray and SZ (Sunyaev-Zel’dovich) surveys of clusters (Stanek et al. 2006; Miyatake et al. 2019; Chiu et al. 2021; Nicola et al. 2020).

We develop a prescription for the cluster assembly bias effect that ties the halo concentration measured by small-scale $\Delta\Sigma$ to the cluster bias measured by either $\Delta\Sigma$ or cluster-galaxy cross-correlation on large scales. By combining cluster conformity with assembly bias, we build an accurate model for the weak lensing profiles $\Delta\Sigma$ of the low and high- M_*^{BCG} clusters across all distance scales. Our conformity+AB model of $\Delta\Sigma$ predicts that the high- M_*^{BCG} clusters have ~20% more concentrated ($c=6.95$) dark matter haloes, but are ~10% less biased ($b=2.85$) than the low- M_*^{BCG} clusters ($c=5.87$ and $b=3.11$), in good agreement with the observations. Using the average membership distance as a proxy of the background contamination, we demonstrate that the impact of projection effects on the inferred conformity and assembly bias signal is likely small (Zu et al. 2017; Busch & White 2017; Sunayama et al. 2020).

We argue that a simple picture of the two-phase BCG-halo co-evolution can explain the complex connection between M_*^{BCG} , λ , and c at fixed halo mass, i.e., M_*^{BCG} is positively correlated with both c and λ despite the anti-correlation between c and λ . In this simple picture, the starbursting phase of the BCG *in situ* growth is induced by the rapid accretion and frequent mergers that built up the central core of the cluster haloes at high redshift, while the *ex situ* BCG stellar mass growth at late times is predominantly driven by the dry mergers with the massive satellites that sunk into the cluster centres via dynamical friction. Consequently, the *in situ* portion of M_*^{BCG} is tied to the halo concentration, while the *ex situ* portion of M_*^{BCG} naturally correlates with the richness of satellite galaxies. A simple

toy model based on this physical picture can qualitatively reproduces the salient features of the observed $M_*^{\text{BCG}} - c - \lambda$ connection.

The strength of the inferred conformity signal may depend on the cluster finder, especially the centroiding algorithm and the definition of richness. We plan to extend our analysis to other publicly-available cluster catalogues, e.g., the Yang et al. (2021) halo-based group catalogue from DECaLS imaging (see also Tinker 2020; Zou et al. 2021) and the Wen & Han (2021) cluster catalogue based on HSC and WISE. Furthermore, the conformity signal could also depend on cosmology. Murata et al. (2019) showed that while the constraints on the mean richness-halo mass relation are consistent between the *Planck* and *WMAP* models, the best-fitting scatter for *Planck* is progressively larger than the *WMAP* model for lower-mass haloes. However, the conformity signal is primarily constrained by the dependence of average halo mass on M_*^{BCG} at fixed richness, therefore should be less affected by the size of the scatter in the richness-halo mass relation.

With the ever-increasing precision of cluster weak lensing measurements (Mandelbaum 2018), we will be able to routinely measure not only the average halo mass of clusters, but also the average halo concentration robustly from the shape of $\Delta\Sigma$ on small scales, after marginalising over the mis-centring (Zhang et al. 2019) and baryonic effects (Cromer et al. 2021). Meanwhile, the diminishing statistical uncertainties of cluster surveys demand a thorough physical understanding of the galaxy-halo connection at the high mass end, which would greatly mitigate the systematic uncertainties in cluster cosmology (Wu et al. 2019, 2021) via the making of more realistic synthetic clusters (Varga et al. 2021). More important, an observationally-motivated yet physically-comprehensive model of galaxy-halo connection, e.g., an extension to our toy model of the $M_*^{\text{BCG}} - c - \lambda$ connection in §6.3, could point us to a minimum-scatter proxy of halo mass (Palmese et al. 2020; Bradshaw et al. 2020; Farahi et al. 2020; Tinker et al. 2021). Therefore, it is imperative that we incorporate the strong conformity and assembly bias effect into the modelling of galaxy-halo connection and weak lensing of clusters for next-generation cluster surveys, including the Rubin Observatory Legacy Survey of Space and Time (LSST; Ivezić et al. 2019), *Euclid* (Laureijs et al. 2011), Chinese Survey Space Telescope (CSST; Gong et al. 2019), and the Roman Space Telescope (Roman; Spergel et al. 2015).

DATA AVAILABILITY

The data underlying this article will be shared on reasonable request to the corresponding author.

ACKNOWLEDGEMENTS

We thank the anonymous referee for the helpful suggestions that have greatly improved this manuscript. We thank Weiguang Cui, Melanie Simet, and Rachel Mandelbaum for helpful discussions. We gracefully thank Christopher Conselice for suggesting the term “cluster conformity” for describing the correlation between BCG and satellites. YZ acknowledges the support by the National Key Basic Research and Development Program of China (No. 2018YFA0404504), National Science Foundation of China (11873038, 11621303, 11890692, 12173024), the science research grants from the China Manned Space Project (No. CMS-CSST-2021-A01, CMS-CSST-2021-B01), the National One-Thousand Youth Talent Program of China, and the SJTU start-up fund (No. WF220407220). YZ and

YPJ acknowledge the support by the 111 Project of the Ministry of Education under grant No. B20019. YZ thanks the wonderful hospitality by Cathy Huang during his visit at the Zhangjiang Hi-Tech Park during the summer of 2021.

REFERENCES

- Abbott T. M. C., et al., 2020, *Phys. Rev. D*, **102**, 023509
- Aihara H., et al., 2011, *ApJS*, **193**, 29
- Aihara H., et al., 2018, *PASJ*, **70**, S4
- Alam S., et al., 2015, *ApJS*, **219**, 12
- Barnes J. E., Hernquist L. E., 1991, *ApJ*, **370**, L65
- Behroozi P. S., Conroy C., Wechsler R. H., 2010, *ApJ*, **717**, 379
- Behroozi P. S., Wechsler R. H., Conroy C., 2013, *ApJ*, **770**, 57
- Boylan-Kolchin M., Ma C.-P., Quataert E., 2008, *MNRAS*, **383**, 93
- Bradshaw C., Leauthaud A., Hearin A., Huang S., Behroozi P., 2020, *MNRAS*, **493**, 337
- Bruzual G., Charlot S., 2003, *MNRAS*, **344**, 1000
- Bundy K., Leauthaud A., Saito S., Maraston C., Wake D. A., Thomas D., 2017, *ApJ*, **851**, 34
- Burke C., Collins C. A., 2013, *MNRAS*, **434**, 2856
- Busch P., White S. D. M., 2017, *MNRAS*, **470**, 4767
- Calderon V. F., Berlind A. A., Sinha M., 2018, *MNRAS*, **480**, 2031
- Carbone C., Fedeli C., Moscardini L., Cimatti A., 2012, *J. Cosmology Astropart. Phys.*, **2012**, 023
- Cataneo M., Rapetti D., 2018, *International Journal of Modern Physics D*, **27**, 1848006
- Chabrier G., 2003, *PASP*, **115**, 763
- Chandrasekhar S., 1943, *ApJ*, **97**, 255
- Chen Y.-M., et al., 2012, *MNRAS*, **421**, 314
- Chen X., Zu Y., Shao Z., Shan H., 2021, arXiv e-prints, p. arXiv:2112.03934
- Chiu I.-N., et al., 2021, arXiv e-prints, p. arXiv:2107.05652
- Collins C. A., et al., 2009, *Nature*, **458**, 603
- Contini E., Yi S. K., Kang X., 2018, *MNRAS*, **479**, 932
- Contreras S., Chaves-Montero J., Zennaro M., Angulo R. E., 2021, arXiv e-prints, p. arXiv:2105.05854
- Cooray A., Sheth R., 2002, *Phys. Rep.*, **372**, 1
- Costanzi Alunno Cerbolini M., Sartoris B., Xia J.-Q., Biviano A., Borgani S., Viel M., 2013, *J. Cosmology Astropart. Phys.*, **2013**, 020
- Costanzi M., et al., 2019a, *MNRAS*, **482**, 490
- Costanzi M., et al., 2019b, *MNRAS*, **488**, 4779
- Cromer D., Battaglia N., Miyatake H., Simet M., 2021, arXiv e-prints, p. arXiv:2104.06925
- Dawson K. S., et al., 2013, *AJ*, **145**, 10
- De Lucia G., Blaizot J., 2007, *MNRAS*, **375**, 2
- Dey A., et al., 2019, *AJ*, **157**, 168
- Fabian A. C., 1994, *ARA&A*, **32**, 277
- Farahi A., Ho M., Trac H., 2020, *MNRAS*, **493**, 1361
- Foreman-Mackey D., Hogg D. W., Lang D., Goodman J., 2013, *PASP*, **125**, 306
- Gao L., Springel V., White S. D. M., 2005, *MNRAS*, **363**, L66
- Giocoli C., Tormen G., Sheth R. K., van den Bosch F. C., 2010, *MNRAS*, **404**, 502
- Golden-Marx J. B., et al., 2021, arXiv e-prints, p. arXiv:2107.02197
- Gong Y., et al., 2019, *ApJ*, **883**, 203
- Grandis S., et al., 2021, *MNRAS*, **504**, 1253
- Groenewald D. N., Skelton R. E., Gilbank D. G., Loubser S. I., 2017, *MNRAS*, **467**, 4101
- Guo H., Yang X., Lu Y., 2018, *ApJ*, **858**, 30
- Hayashi E., White S. D. M., 2008, *MNRAS*, **388**, 2
- Hopkins P. F., Cox T. J., Hernquist L., Narayanan D., Hayward C. C., Murray N., 2013, *MNRAS*, **430**, 1901
- Ivezic Z., et al., 2019, *ApJ*, **873**, 111
- Jiang C. Y., Jing Y. P., Faltenbacher A., Lin W. P., Li C., 2008, *ApJ*, **675**, 1095
- Jing Y., 2019, *Science China Physics, Mechanics, and Astronomy*, **62**, 19511
- Jing Y. P., Suto Y., Mo H. J., 2007, *ApJ*, **657**, 664
- Kauffmann G., Li C., Heckman T. M., 2010, *MNRAS*, **409**, 491
- Klypin A. A., Trujillo-Gomez S., Primack J., 2011, *ApJ*, **740**, 102
- Klypin A., Yepes G., Gottlöber S., Prada F., Heß S., 2016, *MNRAS*, **457**, 4340
- Knobel C., Lilly S. J., Woo J., Kovač K., 2015, *ApJ*, **800**, 24
- Lam T. Y., Nishimichi T., Schmidt F., Takada M., 2012, *Phys. Rev. Lett.*, **109**, 051301
- Laporte C. F. P., White S. D. M., Naab T., Gao L., 2013, *MNRAS*, **435**, 901
- Laureijs R., et al., 2011, arXiv e-prints, p. arXiv:1110.3193
- Lavoie S., et al., 2016, *MNRAS*, **462**, 4141
- Lazeyras T., Villaescusa-Navarro F., Viel M., 2021, *J. Cosmology Astropart. Phys.*, **2021**, 022
- Lidman C., et al., 2013, *MNRAS*, **433**, 825
- Lin Y.-T., et al., 2017, *ApJ*, **851**, 139
- Liu F. S., Mao S., Deng Z. G., Xia X. Y., Wen Z. L., 2009, *MNRAS*, **396**, 2003
- Mancone C. L., Gonzalez A. H., 2012, *PASP*, **124**, 606
- Mandelbaum R., 2018, *ARA&A*, **56**, 393
- Mandelbaum R., Wang W., Zu Y., White S., Henriques B., More S., 2016, *MNRAS*, **457**, 3200
- Mandelbaum R., et al., 2018, *PASJ*, **70**, S25
- Maraston C., Strömbäck G., Thomas D., Wake D. A., Nichol R. C., 2009, *MNRAS*, **394**, L107
- McDonald M., et al., 2012, *Nature*, **488**, 349
- McDonald M., et al., 2016, *ApJ*, **817**, 86
- Mihos J. C., Hernquist L., 1996, *ApJ*, **464**, 641
- Miyatake H., More S., Takada M., Spergel D. N., Mandelbaum R., Rykoff E. S., Rozo E., 2016, *Phys. Rev. Lett.*, **116**, 041301
- Miyatake H., et al., 2019, *ApJ*, **875**, 63
- Murante G., Giovalli M., Gerhard O., Arnaboldi M., Borgani S., Dolag K., 2007, *MNRAS*, **377**, 2
- Murata R., Nishimichi T., Takada M., Miyatake H., Shirasaki M., More S., Takahashi R., Osato K., 2018, *ApJ*, **854**, 120
- Murata R., et al., 2019, *PASJ*, **71**, 107
- Myles J., et al., 2021, *MNRAS*, **505**, 33
- Nicola A., Dunkley J., Spergel D. N., 2020, *Phys. Rev. D*, **102**, 083505
- Oogi T., Habe A., Ishiyama T., 2016, *MNRAS*, **456**, 300
- Ostriker J. P., Hausman M. A., 1977, *ApJ*, **217**, L125
- Palmese A., et al., 2020, *MNRAS*, **493**, 4591
- Paranjape A., Kovač K., Hartley W. G., Pahwa I., 2015, *MNRAS*, **454**, 3030
- Phillips J. I., Wheeler C., Boylan-Kolchin M., Bullock J. S., Cooper M. C., Tollerud E. J., 2014, *MNRAS*, **437**, 1930
- Planck Collaboration et al., 2020, *A&A*, **641**, A6
- Prada F., Klypin A. A., Cuesta A. J., Betancort-Rijo J. E., Primack J., 2012, *MNRAS*, **423**, 3018
- Robotham A. S. G., et al., 2013, *MNRAS*, **431**, 167
- Rozo E., et al., 2010, *ApJ*, **708**, 645
- Rozo E., Rykoff E. S., Becker M., Reddick R. M., Wechsler R. H., 2015, *MNRAS*, **453**, 38
- Ruszkowski M., Springel V., 2009, *ApJ*, **696**, 1094
- Rykoff E. S., et al., 2014, *ApJ*, **785**, 104
- Salcedo A. N., Wibking B. D., Weinberg D. H., Wu H.-Y., Ferrer D., Eisenstein D., Pinto P., 2020, *MNRAS*, **491**, 3061
- Sartoris B., et al., 2016, *MNRAS*, **459**, 1764
- Simet M., McClintock T., Mandelbaum R., Rozo E., Rykoff E., Sheldon E., Wechsler R. H., 2017, *MNRAS*, **466**, 3103
- Spergel D., et al., 2015, arXiv e-prints, p. arXiv:1503.03757
- Stanek R., Evrard A. E., Böhringer H., Schuecker P., Nord B., 2006, *ApJ*, **648**, 956
- Sunayama T., et al., 2020, *MNRAS*, **496**, 4468
- Takahashi R., Sato M., Nishimichi T., Taruya A., Oguri M., 2012, *ApJ*, **761**, 152
- Tinker J. L., 2020, arXiv e-prints, p. arXiv:2007.12200
- Tinker J., Kravtsov A. V., Klypin A., Abazajian K., Warren M., Yepes G., Gottlöber S., Holz D. E., 2008, *ApJ*, **688**, 709
- Tinker J. L., Robertson B. E., Kravtsov A. V., Klypin A., Warren M. S., Yepes G., Gottlöber S., 2010, *ApJ*, **724**, 878

- Tinker J. L., Cao J., Alpaslan M., DeRose J., Mao Y.-Y., Wechsler R. H., 2021, *MNRAS*, **505**, 5370
- To C.-H., Reddick R. M., Rozo E., Rykoff E., Wechsler R. H., 2020, *ApJ*, **897**, 15
- Umetsu K., 2020, *A&ARv*, **28**, 7
- Varga T. N., et al., 2021, arXiv e-prints, p. arXiv:2102.10414
- Vulcani B., et al., 2016, *ApJ*, **816**, 86
- Webb T. M. A., et al., 2015, *ApJ*, **814**, 96
- Weinberg D. H., Mortonson M. J., Eisenstein D. J., Hirata C., Riess A. G., Rozo E., 2013, *Phys. Rep.*, **530**, 87
- Wu H.-Y., Weinberg D. H., Salcedo A. N., Wibking B. D., Zu Y., 2019, *MNRAS*, **490**, 2606
- Wu H.-Y., Weinberg D. H., Salcedo A. N., Wibking B. D., 2021, *ApJ*, **910**, 28
- Weinmann S. M., van den Bosch F. C., Yang X., Mo H. J., 2006, *MNRAS*, **366**, 2
- Wen Z. L., Han J. L., 2021, *MNRAS*, **500**, 1003
- Wetzel A. R., White M., 2010, *MNRAS*, **403**, 1072
- Whiley I. M., et al., 2008, *MNRAS*, **387**, 1253
- White S. D. M., 1976, *MNRAS*, **174**, 19
- Xu K., Zheng Y., Jing Y., 2021, arXiv e-prints, p. arXiv:2109.11738
- Yang X., Mo H. J., van den Bosch F. C., Pasquali A., Li C., Barden M., 2007, *ApJ*, **671**, 153
- Yang X., Mo H. J., van den Bosch F. C., Bonaca A., Li S., Lu Y., Lu Y., Lu Z., 2013, *ApJ*, **770**, 115
- Yang X., et al., 2021, *ApJ*, **909**, 143
- York D. G., et al., 2000, *AJ*, **120**, 1579
- Zhang Y., et al., 2019, *MNRAS*, **487**, 2578
- Zhao D. H., Mo H. J., Jing Y. P., Börner G., 2003, *MNRAS*, **339**, 12
- Zhao D. H., Jing Y. P., Mo H. J., Börner G., 2009, *ApJ*, **707**, 354
- Zhao D., Conselice C. J., Aragón-Salamanca A., Almaini O., Hartley W. G., Lani C., Mortlock A., Old L., 2017, *MNRAS*, **464**, 1393
- Zou H., et al., 2021, *ApJS*, **253**, 56
- Zu Y., Mandelbaum R., 2015, *MNRAS*, **454**, 1161
- Zu Y., Mandelbaum R., 2016, *MNRAS*, **457**, 4360
- Zu Y., Mandelbaum R., 2018, *MNRAS*, **476**, 1637
- Zu Y., Weinberg D. H., Rozo E., Sheldon E. S., Tinker J. L., Becker M. R., 2014a, *MNRAS*, **439**, 1628
- Zu Y., Weinberg D. H., Jennings E., Li B., Wyman M., 2014b, *MNRAS*, **445**, 1885
- Zu Y., Mandelbaum R., Simet M., Rozo E., Rykoff E. S., 2017, *MNRAS*, **470**, 551
- Zu Y., et al., 2021, *MNRAS*, **505**, 5117

APPENDIX A: A PRESCRIPTION FOR CLUSTER ASSEMBLY BIAS

To calibrate an accurate prescription of cluster assembly bias, we employ a large-volume high-resolution cosmological N -body simulation from the CosmicGrowth suite developed by Jing (2019). In particular, we utilize the $z=0.23$ (closest to the mean redshift of our cluster sample) snapshot of the Planck_2048_1200 simulation, which has a box-length of $1.2 \text{ Gpc}/h$ and a mass resolution of $1.76 \times 10^{10} h^{-1} M_{\odot}$ at Planck cosmology. We refer readers to Jing (2019) for technical details of the simulation. We identify dark matter haloes using the spherical overdensity-based ROCKSTAR (Behroozi et al. 2013) halo finder, and compute halo concentrations using the maximum circular velocity-based approach (Klypin et al. 2011; Prada et al. 2012).

We select all the haloes with mass between $10^{13} - 10^{15} h^{-1} M_{\odot}$ and divide them into six bins in halo mass. Within each halo mass bin, we measure the median \bar{c} and scatter σ_c of the concentration distribution, and select the haloes within $\pm 2\sigma_c$ into four concentration bins with equal $1-\sigma_c$ widths. We then measure the 3D isotropic halo-matter cross-correlation functions ξ_{hm} by cross-correlating the positions of haloes with that of dark matter particles, as shown in

Figure A1. The six panels of Figure A1 present the ξ_{hm} measurements for the six halo mass bins of $\lg M_h = 13-13.29$, $13.29-13.57$, $13.57-13.86$, $13.86-14.14$, $14.14-14.43$, and $14.43-15$, respectively. In each panel, the main sub-panel shows the ξ_{hm} of haloes in four concentration bins, $[-2\sigma_c, \sigma_c]$ (red), $[-\sigma_c, 0]$ (orange), $[0, \sigma_c]$ (cyan), and $[\sigma_c, 2\sigma_c]$ (purple), as well as the measurement for all the haloes in that mass bin (gray with errorbars). The division of concentration bins is indicated by the concentration distribution in the inset panel, with each coloured segment mapped to one of the four concentration bins. We plot $r^2 \xi_{\text{hm}}$ instead of ξ_{hm} in the y-axis to highlight the differences between the four concentration bins on both the small and large scales. The bottom sub-panel shows the ratio between the ξ_{hm} profile of each concentration bin and that of the all the haloes in that mass bin. We compute the uncertainties of ξ_{hm} and their ratios with Jackknife re-sampling, though we do not show the errorbars (except for the gray curves) in Figure A1 to avoid clutter.

The dependence of ξ_{hm} on halo concentration is consistent across all mass bins, with the low-concentration haloes showing stronger biases than the high-concentration systems. The probability distributions of concentration are reasonably Gaussian, with some level of skewness and kurtosis developed for the higher mass bins. The lowest mass bin, however, does show a narrower range of variation of bias with concentration, as the concentration-bias relation would reverse its sign below the characteristic non-linear mass scale, i.e., low-concentration haloes would be less biased in the low halo mass regime (Gao et al. 2005). There, we drop the lowest mass bin of Figure A1 from our assembly bias calibration. To accurately calibrate assembly bias well into the characteristic non-linear mass scale, a suite of extremely high-resolution simulations that can resolve haloes down to $10^{11} h^{-1} M_{\odot}$ is required, hence beyond the scope of this paper. Nonetheless, since the main bulk of the halo mass distribution of our cluster sample is above $\lg M_h = 13.29$ (see Figure 5), the systematic uncertainty of our assembly bias model caused by the omission of low mass haloes should be small compared to the observational errors.

Given the similarities of assembly bias across the cluster mass range, we can normalize the values of concentration and bias to remove the general trend of c and b with halo mass. From each bin of (M_h, c) in Figure A1, we can calculate the relative concentrations \hat{c} as

$$\hat{c}(M_h, c) = \frac{c - \bar{c}(M_h)}{\sigma_c(M_h)}, \quad (\text{A1})$$

and the relative bias $\hat{b}(M_h, c)$ as

$$\hat{b}(M_h, c) = \frac{b(M_h, c) - \bar{b}(M_h)}{\bar{b}(M_h)}, \quad (\text{A2})$$

where \bar{b} is the average halo bias of that halo mass. We calculate the biases using the ξ_{hm} measurements on scales between $10h^{-1} \text{ Mpc}$ and $30h^{-1} \text{ Mpc}$, and the errorbars on \hat{b} with Jackknife re-sampling technique.

Figure A2 shows our result of the cluster assembly bias measurement in the form of $\hat{b}-\hat{c}$ relation in five different halo mass bins of $13.29-13.57$, $13.57-13.86$, $13.86-14.14$, $14.14-14.43$, and $14.43-15.00$, respectively. The relative bias exhibits a declining trend with \hat{c} , reproducing the standard halo assembly bias phenomenon, i.e., an anti-correlation between concentration and bias in the cluster mass regime (Jing et al. 2007). More important, the five $\hat{b}(\hat{c})$ measurements are consistent with each other, suggesting a universal $\hat{b}-\hat{c}$ relation that is roughly independent of halo mass at $\lg M_h > 13.29$. As a result, we are able to fit a simple 3rd order polynomial to the five mass bins simultaneously, yielding the black solid curve as our

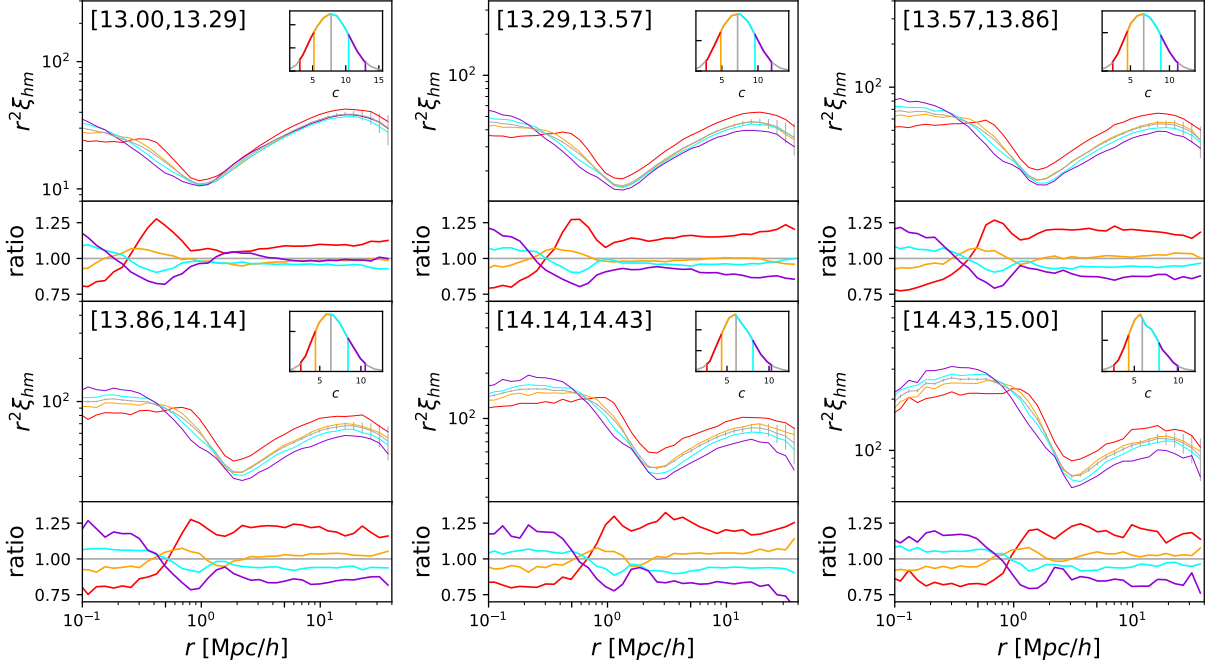


Figure A1. Dependence of the 3D isotropic halo-matter cross-correlation function ξ_{hm} on concentration in six halo mass bins ranging from $10^{13} h^{-1} M_{\odot}$ to $10^{15} h^{-1} M_{\odot}$ (increasing from left to right and from top to bottom). For each mass bin, the main sub-panel compares the ξ_{hm} of haloes in four concentration bins, $[-2\sigma_c, \sigma_c]$ (red), $[-\sigma_c, 0]$ (orange), $[0, \sigma_c]$ (cyan), and $[\sigma_c, 2\sigma_c]$ (purple), illustrated by the four segments of concentration distribution in the inset panel. We plot $r^2 \xi_{\text{hm}}$ instead of ξ_{hm} in the y-axes to highlight the difference between the four concentration bins on all distance scales. Gray curve with errorbars indicates the ξ_{hm} of all the haloes in that mass bin. The bottom sub-panel shows the ratio profiles between the ξ_{hm} of four concentration bins and that of all haloes in the same mass bin. We calculate halo biases from the ξ_{hm} measurements on scales between $10 h^{-1} \text{Mpc}$ and $30 h^{-1} \text{Mpc}$, where the biases are roughly linear.

prescription for the halo assembly bias in our cluster sample,

$$\hat{b} = -0.027\hat{c}^3 + 0.026\hat{c}^2 - 0.084\hat{c} - 0.019. \quad (\text{A3})$$

Equation A3 has a χ^2 per degree of freedom of ~ 0.8 , indicating a reasonably good description of the simulation measurements. Note that Equation A3 does not go through $(0, 0)$, due to the fact that the concentration distribution at fixed M_h is often slightly skewed. Although our prescription is calibrated at *Planck* cosmology, it is likely that the same parameters would still work for other cosmologies (Contreras et al. 2021; Lazeyras et al. 2021).

APPENDIX B: A JOINT MODEL OF CONFORMITY AND ASSEMBLY BIAS FOR $\Delta\Sigma$

We are now ready to construct a comprehensive model of the cluster weak lensing profile $\Delta\Sigma$ by incorporating both the BCG-satellite conformity constrained in §4.3 and the cluster assembly bias calibrated in Figure A2. In particular, in §5 we demonstrate the efficacy of our $\Delta\Sigma$ models by comparing their predicted full weak lensing profiles of the low and high- M_{*}^{BCG} subsamples to the measurements from Paper I. We predict $\Delta\Sigma$ for the two cluster subsamples in two separate steps, with cluster assembly bias modelled in the first step and the BCG-satellite conformity modelled in the second. We describe each step in turn below.

In the first step, we predict $\Delta\Sigma$ as a function of the projected distance r_p for haloes at fixed mass M_h and concentration c ,

$$\Delta\Sigma(r_p | M_h, c) = \bar{\Sigma}(\langle r_p | M_h, c \rangle) - \Sigma(r_p | M_h, c), \quad (\text{B1})$$

where $\bar{\Sigma}(\langle r_p | M_h, c \rangle)$ and $\Sigma(r_p | M_h, c)$ are the average surface matter density interior to and at radius r_p , respectively. In the absence of mis-centring, $\Sigma(r_p)$ can be predicted by integrating the 3D isotropic halo-mass cross-correlation function $\xi_{\text{hm}}(r)$ over the line of sight distance r_{π} ,

$$\Sigma(r_p | M_h, c) = \rho_m \int_{-\infty}^{+\infty} \xi_{\text{hm}} \left(\sqrt{r_p^2 + r_{\pi}^2} | M_h, c \right) dr_{\pi}, \quad (\text{B2})$$

where ρ_m is the mean density of the Universe and we use $\pm 100 h^{-1} \text{Mpc}$ for the integration limit instead of $\pm\infty$ in practice.

Following Paper I, we describe the mis-centring effect using the fraction of BCGs mis-centred f_{off} and their offsets from the true centres r_{off} , which follows a shape-2 Gamma distribution $p(r_{\text{off}})$ with a characteristic offset σ_{off} ,

$$p(r_{\text{off}}) = \frac{r_{\text{off}}}{\sigma_{\text{off}}^2} \exp\left(-\frac{r_{\text{off}}}{\sigma_{\text{off}}}\right). \quad (\text{B3})$$

The observed surface matter density in the presence of mis-centring is thus

$$\Sigma^{\text{obs}}(r_p | M_h, c) = f_{\text{off}} \Sigma^{\text{off}}(r_p | M_h, c) + (1 - f_{\text{off}}) \Sigma(r_p | M_h, c), \quad (\text{B4})$$

where

$$\Sigma^{\text{off}}(r_p) = \frac{1}{2\pi} \int_0^{\infty} dr_{\text{off}} p(r_{\text{off}}) \int_0^{2\pi} d\theta \Sigma \left(\sqrt{r_p^2 + r_{\text{off}}^2 - 2r_p r_{\text{off}} \cos \theta} \right). \quad (\text{B5})$$

We adopt the best-fitting values of f_{off} (0.37 vs. 0.20 for low and

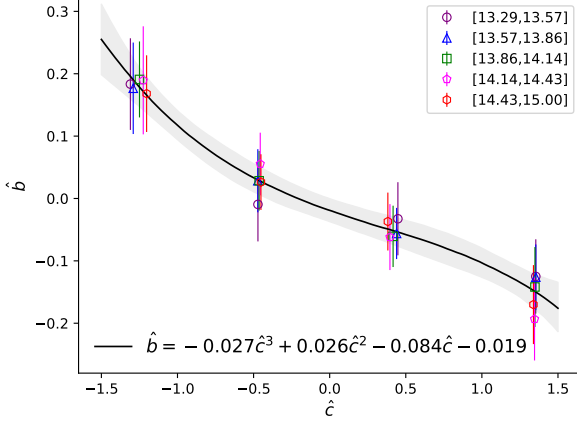


Figure A2. Our prescription of the cluster assembly bias calibrated for haloes at $z \approx 0.23$. Symbols of different colours with errorbars indicate the measurements of the relative bias \hat{b} (Equation A2) as a function of the relative concentration \hat{c} (Equation A1) in five different halo mass bins indicated by the legend in the top right. Black solid line is our 3rd-order polynomial fit to the data points, with the best-fitting parameters indicated in the bottom left.

high- M_*^{BCG} subsamples) and σ_{off} (0.23 vs. $0.21 h^{-1} \text{Mpc}$ for low and high) listed in the table 1 of Paper I. For our current analysis, we assume that both offset parameters are independent of halo mass for simplicity, but expect to incorporate M_h -dependent mis-centring models for future observations.

To calculate $\Sigma(r_p | M_h, c)$, we adopt the ξ_{hm} model developed by Zu et al. (2014a) (a modified version proposed by Hayashi & White 2008),

$$\begin{aligned} \xi_{\text{hm}}(r | M_h, c) &= \begin{cases} \xi_{1\text{h}} & \text{if } \xi_{1\text{h}} \geq \xi_{2\text{h}}, \\ \xi_{2\text{h}} & \text{if } \xi_{1\text{h}} < \xi_{2\text{h}}, \end{cases} \\ \xi_{1\text{h}} &= \frac{\rho_{\text{NFW}}(r | M_h, c)}{\rho_{\text{m}}} - 1, \\ \xi_{2\text{h}} &= b(M_h, c) \xi_{\text{mm}}. \end{aligned} \quad (\text{B6})$$

Here $\xi_{1\text{h}}$ and $\xi_{2\text{h}}$ are the so-called “1-halo” and “2-halo” terms in the halo model (Cooray & Sheth 2002), $\rho_{\text{NFW}}(r | M_h, c)$ is the NFW density profile of a halo with mass M_h and concentration c , $b(M_h, c)$ is the large-scale bias of that halo, and ξ_{mm} is the non-linear matter-matter auto-correlation function predicted at *Planck* cosmology (Takahashi et al. 2012). Zu et al. (2014a) found that Equation B6 provides an adequate description of the halo-matter cross-correlation functions measured from simulations, though for future surveys it is more preferred to switch to an emulator-based approach for predicting ξ_{hm} for better accuracy (Salcedo et al. 2020).

By applying our cluster assembly bias prescription calibrated in §A, we can accurately predict $b(M_h, c)$ as

$$b(M_h, c) \equiv b(M_h, \hat{c}) = \bar{b}(M_h) \left(1 + \hat{b}(\hat{c}) \right), \quad (\text{B7})$$

where $\hat{b}(\hat{c})$ is the assembly bias relation of Equation A3. We adopt the fitting formulae for the mean concentration–mass $\bar{c}(M_h)$ and bias–mass $\bar{b}(M_h)$ relations from Zhao et al. (2009) and Tinker et al. (2010), respectively.

After obtaining the prediction for $\Delta\Sigma(r_p | M_h, c)$, in the second step we derive the weak lensing profiles of the high and low- M_*^{BCG} cluster subsamples (hereafter referred to as S_*^+ and S_*^- , respectively)

by integrating $\Delta\Sigma(r_p | M_h, c)$ over the underlying halo distribution $p(M_h, c | S_*^\pm)$

$$\Delta\Sigma(r_p | S_*^\pm) = \iint \Delta\Sigma(r_p | M_h, c) p(M_h, c | S_*^\pm) dc dM_h. \quad (\text{B8})$$

The 2D PDF $p(M_h, c | S_*^\pm)$ can be rewritten as

$$p(M_h, c | S_*^\pm) = p(c | M_h, S_*^\pm) p(M_h | S_*^\pm), \quad (\text{B9})$$

where $p(M_h | S_*^\pm)$ can be derived from Equation 15 and is shown in the bottom (top) right panel of Figure 5 for each of the two subsamples predicted by the (anti-)conformity model.

The concentration distribution $p(c | M_h, S_*^\pm)$, however, is very challenging to infer from the current weak lensing measurements. We can nonetheless simplify the problem as follows. Paper I discovered that the high- M_*^{BCG} clusters have a higher average concentration, hence a higher average relative concentration $\langle \hat{c} | M_h \rangle$, than their low- M_*^{BCG} counterparts. If we make a further *ansatz* that the probability distribution of relative concentration \hat{c} is the same at any fixed halo mass for either subsample

$$p(\hat{c} | M_h, S_*^\pm) \equiv p(\hat{c} | S_*^\pm), \quad (\text{B10})$$

so that $\langle \hat{c} | M_h \rangle \equiv \langle \hat{c} \rangle$, then the average concentrations of the high and low- M_*^{BCG} clusters can then be modelled by only two parameters, $\langle \hat{c}_+ \rangle$ and $\langle \hat{c}_- \rangle$, respectively. After switching the variable from c to \hat{c} ,

$$p(c | M_h, S_*^\pm) dc = p(\hat{c} | S_*^\pm) d\hat{c}, \quad (\text{B11})$$

Equation B8 can be rewritten as

$$\Delta\Sigma(r_p | S_*^\pm) = \iint \Delta\Sigma(r_p | M_h, \hat{c}) p(\hat{c} | S_*^\pm) p(M_h | S_*^\pm) d\hat{c} dM_h. \quad (\text{B12})$$

Finally, after integrating out $p(\hat{c} | S_*^\pm)$ in Equation B12, we arrive at our prediction for the stacked weak lensing profile of subsample S_*^\pm

$$\Delta\Sigma(r_p | S_*^\pm) = \int_{M_h^{\text{min}}}^{M_h^{\text{max}}} \Delta\Sigma(r_p | M_h, \langle \hat{c}_\pm \rangle) p(M_h | S_*^\pm) dM_h, \quad (\text{B13})$$

where the cluster assembly bias and BCG-satellite conformity are incorporated into the first and second terms of the integrand, respectively.

Since the halo mass distributions $p(M_h | S_*^\pm)$ can be predicted by Equation 15 for any level of conformity, the only unknown piece in Equation B13 is $\Delta\Sigma(r_p | M_h, \langle \hat{c}_\pm \rangle)$, which we predict as follows. Given a value of $\langle \hat{c}_\pm \rangle$ for subsample S_*^\pm , we can compute the average concentration at fixed halo mass as

$$\langle c | M_h, S_*^\pm \rangle = \langle \hat{c}_\pm \rangle \sigma_c + \bar{c}(M_h), \quad (\text{B14})$$

and the average bias at fixed halo mass as

$$\langle b | M_h, S_*^\pm \rangle = \bar{b}(M_h) \left(1 + \hat{b}(\langle \hat{c}_\pm \rangle) \right), \quad (\text{B15})$$

respectively, where $\hat{b}(\langle \hat{c}_\pm \rangle)$ is the cluster assembly bias we derived in Equation A3.

To obtain a good description of the measured cluster weak lensing profiles on small scales, we adjust the values of $\langle \hat{c}_\pm \rangle$ so that the average concentration of each subsample is consistent with the best-fitting average halo concentrations derived in Paper I, i.e., $\langle c_- \rangle = 5.87$ for the low- M_*^{BCG} and $\langle c_+ \rangle = 6.95$ for the high- M_*^{BCG} subsamples, respectively. Assuming the mean concentration–mass relation from Zhao et al. (2009) and a constant concentration scatter of

$\sigma_c=0.15$, our best-fitting values are $\langle\hat{c}_-\rangle=0.156$ and $\langle\hat{c}_+\rangle=1.045$ within the posterior mean conformity model, while in the anti-conformity model they become $\langle\hat{c}_-\rangle=0.17$ and $\langle\hat{c}_+\rangle=1.206$. By applying those values of $\langle c_{\pm}\rangle$, we can further infer the bias values via the cluster assembly bias prescription of Equation A3. In particular, within the conformity model, the biases are $\langle b_+\rangle=3.20$ and $\langle b_-\rangle=3.21$ when cluster assembly bias is switched off, and $\langle b_+\rangle=2.85$ and $\langle b_-\rangle=3.11$ when cluster Assembly bias is on, respectively. We also infer $\langle b_+\rangle=3.78$ and $\langle b_-\rangle=2.79$ for the anti-conformity but without applying cluster assembly bias, because the model is already ruled out regardless of the existence of cluster assembly bias. We adopt those best-fitting values of $\langle\hat{c}_{\pm}\rangle$ and $\langle b_{\pm}\rangle$ and predict the $\Delta\Sigma$ profiles for the low and high- M_{*}^{BCG} subsamples under different assumptions of conformity and assembly bias.

This paper has been typeset from a \TeX/L\AA\TeX file prepared by the author.